

Measuring the seismic properties of Tibetan bright spots: Evidence for free aqueous fluids in the Tibetan middle crust

Yizhaq Makovsky¹ and Simon L. Klemperer

Department of Geophysics, Stanford University, Stanford, California

Abstract. Seismic bright spots are commonly interpreted to mark fluid concentrations, but their nature (melt or aqueous) is usually inferred only from circumstantial evidence of the geologic setting. A band of bright spot reflections has been imaged by Project INDEPTH (International Deep Profiling of Tibet and the Himalayas) at about 15 km depth along 150 km of the northern Yadong-Gulu rift, southern Tibet. We use INDEPTH three-component wide-angle seismic data to measure seismic velocities at the bright spot reflector, and theoretical rock physics bounds to constrain the nature of the fluids. Merging of data from multiple bright spots allows us to use a one-dimensional approximation. Travel time modeling yields average P and S velocities for the upper crust above the bright spots of 5.3 ± 0.2 and 3.2 ± 0.2 km s⁻¹, respectively. Reflection-amplitude variation with offset (AVO) modeling constrains the P and S velocities of the bright spots to 3.0 ± 0.8 and 1.6 ± 0.8 km s⁻¹, respectively. Multiple modeling procedures suggest these velocities are not model dependent. Our results imply that of the order of 10% volume of free aqueous fluids in the Tibetan middle crust produces the observed bright spot reflections. The presence of relatively large quantities of free aqueous fluids, presumably mostly saline supercritical H₂O, does not preclude the presence of melt but does constrain the maximum temperature at the bright spots to the wet granite solidus (about 650°C) and thus the maximum surface heat flow to ≤ 110 mW m⁻². The observed bright spots can alternatively be explained as a result of transient flow of aqueous fluids through a lower temperature and lower heat flow southern Tibetan crust.

1. Introduction

A seismic bright spot is a segment of a reflection on a near-vertical seismic reflection section which exhibits anomalously high reflection amplitudes. Bright spots have long been used in industry as a direct indication for the presence of hydrocarbons, most typically as an indication of a gas-bearing layer at the top of a hydrocarbon trap [e.g., Stone, 1977; Allen and Peddy, 1993]. The analysis of reflection amplitude variation with offset (AVO; discussed below) has been the most important technique used to identify the fluids associated with these bright spots [e.g., Ostrander, 1984; Castagna and Backus, 1993]. In this paper we will use the term bright spots loosely to refer to the reflective bodies generating bright-spot reflections when imaged on vertical-incidence seismic data.

Basement bright spots, or “deep-crustal bright spots,” have been observed in different geological settings around the world (A. R. Ross and L. D. Brown, Seismic bright spots and continental rheology, submitted to *Reviews of Geophysics*, 1998): in mid-ocean ridges 1–2 km below the seafloor [e.g., Hussenoeder *et al.*, 1996]; beneath arc volcanoes at about 5 to 20 km depth [e.g., Hammer and Clowes, 1996; Matsumoto and Hasegawa, 1996; Schilling *et al.*, 1997]; in subduction zones [e.g., Calvert and Clowes, 1990]; from the midcrust to the Moho of continental rifts [e.g., Brown *et al.*, 1987; Jarchow *et al.*, 1993]; in orogens [e.g., Brown *et al.*, 1996; Mandler and Clowes, 1998];

and even in stable midcontinental areas [e.g., Barnes and Reston, 1992; Lüeschen, 1994; Pratt *et al.*, 1993]. Among the geophysical characteristics assigned in the literature to different basement bright spots are the following: anomalously high vertical-incidence P wave reflection amplitudes, usually of the order of 10 dB above background level [e.g., Brown *et al.*, 1987]; negative P wave reflection polarity [e.g., Ryberg and Fuis, 1998]; complex seismic reflection waveform and frequency response suggesting thin layering [e.g., Ake and Sanford, 1988; Brocher, 1981]; diffractive character [e.g., Barnes and Reston, 1992]; distinct S wave reflectivity [e.g., Matsumoto and Hasegawa, 1996; Sanford *et al.*, 1973]; strong P and S converted mode reflections [e.g., Jarchow *et al.*, 1993; Sanford *et al.*, 1977]; low electromagnetic resistivity, as low as 1 to 10 Ω m [e.g., Hyndman and Shearer, 1989; Jones, 1992; Schilling *et al.*, 1997]; S wave anisotropy [e.g., Lüeschen, 1994]; and proximity to areas of high microseismic activity [e.g., Sanford *et al.*, 1973; Cameli *et al.*, 1993]. Interpretations suggested for the nature of the different basement bright spots include melt bodies [e.g., Jarchow *et al.*, 1993; Matsumoto and Hasegawa, 1996; Sanford *et al.*, 1973], aqueous fluid concentrations [e.g., Bailey, 1990], solid mafic bodies [e.g., Pratt *et al.*, 1993], detachments at rheological boundaries [e.g., Jones and Nur, 1984; Cameli *et al.*, 1993; Ryberg and Fuis, 1998], and imaging artifacts. Some of these interpretations are based on investigation of elastic properties [e.g., Pratt *et al.*, 1993], but usually the crucial arguments are based on the geological setting of the bright spots. Without exception, the nature of fluids in continental basement has previously been inferred to be magmatic or aqueous based primarily on heat flow measurements and evidence for or against recent volcanism. In this paper, uniquely, we explore

¹Now at Paradigm Geophysical, Herzlia, Israel.

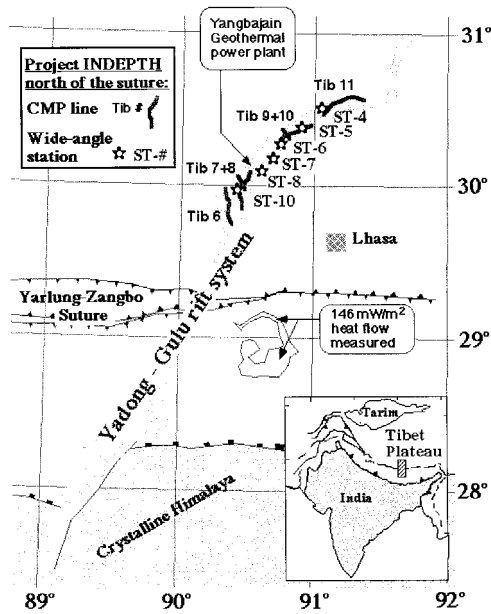


Figure 1. Schematic map of southern Tibet (striped rectangle in the bottom right inset). Note project INDEPTH CMP lines (dark gray lines) and wide-angle stations (stars) in the northern Yadong-Gulu rift (dotted pattern), north of the Yarlung Zangbo suture; structural features of southern Tibet (thin dark lines); the Yarlung-Zangbo (Zangbo = river; thick gray line); Lhasa (patterned square); Yamdrog lake, in which Francheteau *et al.* [1984] measured heat flow of 146 mW m^{-2} ; and the power plant in Yangbajain geothermal field. (For more detailed maps, see Alsdorf *et al.* [1998a].)

the evidence given by direct seismic measurements alone to distinguish aqueous fluids from magma.

In the Tibetan plateau, uplifted subsequent to the India-Asia continental collision along the Yarlung-Zangbo suture (YZS) (Figure 1), the crust has thickened to double the thickness of normal continental crust [Chun and Yoshii, 1977; Hirn *et al.*, 1984; Nelson *et al.*, 1996; Owens and Zandt, 1997]. However, east-west extension along a series of north trending rifts, most prominently the Yadong-Gulu rift, is currently the active de-

formational mode observed at the surface in southern Tibet [Armijo *et al.*, 1986; Harrison *et al.*, 1992; Molnar *et al.*, 1981]. Although many models have been suggested for the evolution and deformation of the Tibetan crust [Willett and Beaumont, 1994, and references therein], the thermal state of this crust, an important aspect and test of these models, is still largely unknown. Hydrothermal activity, including hot springs and fumaroles, is abundant at the surface throughout the Tibetan plateau and, in particular, in the northern Yadong-Gulu rift (north of the YZS) [Wang *et al.*, 1981; Shen *et al.*, 1995]. Anomalously high heat flow of 146 mW m^{-2} was measured in Yamdrog lake about 50 km south of the YZS (Figure 1) and was taken to suggest the presence of magma at less than 20 km depth [Francheteau *et al.*, 1984]. However, Hochstein and Yang [1992, 1995] show that such high values may be measured at the surface as a result of terrain-induced advective flow, in a valley similar to the Yamdrog-lake valley, with a crustal heat flow of only 60 to 90 mW m^{-2} . Heat flow estimates taking into account the advective component, from temperature profiles of deep wells in southern Tibet, vary between 65 mW m^{-2} at Lhasa and 80 to 110 mW m^{-2} in the vicinity of the Yangbajain geothermal plant (Figure 1) and have been interpreted to define a "heat band" along the northern Yadong-Gulu rift [Hochstein and Yang, 1995; Hochstein and Regenauer-Lieb, 1998]. The high surface heat flow values and their variability may be a result of heat convection in a deep-reaching hydrothermal system [Taylor, 1990; Wickham, 1992] and may not reliably constrain the thermal state of the Tibetan crust. Upper mantle earthquakes at a depth range of about 70 to 113 km [Molnar and Chen, 1983; Zhu and Helmberger, 1996] imply a relatively cool boundary condition $<750^\circ\text{C}$ for the base of the Tibetan crust (C. Ruppel and D. McNamara, Seismic and rheological constraints on absolute temperature in the Tibetan-plateau upper mantle, submitted to *Earth and Planetary Science Letters*, 1998).

An undulating band of P wave reflections (here named P_xP following Sanford *et al.* [1973]), locally exhibiting bright-spot characteristics (high reflection amplitude and negative reflection polarity), was serendipitously imaged at 5- to 6-s two-way travel time (tw) by INDEPTH (International Deep Profiling of Tibet and the Himalayas) common midpoint (CMP) profiles

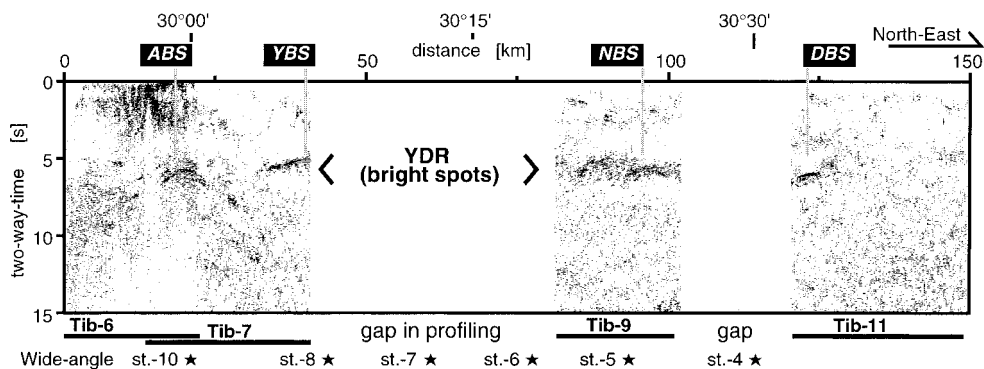


Figure 2a. INDEPTH 15-fold stacked section (unmigrated) of CMP profile segments Tib-6 to 11 [after Brown *et al.*, 1996]. The extent of each reflection-profile segment is noted below the sections, together with location of wide-angle stations (stars). Distances along a northeast line are noted above. An undulating about 2-s two-way travel time (tw) wide band of reflectivity (Yamdrog-Damxung reflector (YDR)) locally exhibiting bright-spot characteristics, is imaged at 5- to 6-s tw. Bright-spot groups: ABS-Angang bright spot; YBS-Yangbajain bright spot; NBS-Nyinzhong bright spot; DBS-Damxung bright spot. Reprinted with permission from Brown *et al.* [1996]. Copyright 1996 American Association for the Advancement of Science.

beneath much of their 150 km route along the northern Yadong-Gulu rift (north of the IYS), southern Tibet [Brown *et al.*, 1996; Alsdorf *et al.*, 1998a, b] (Figures 1 and 2). High-amplitude P to S converted reflections (P_xS ; Plate 1) recorded by our INDEPTH wide-angle experiment [Makovsky *et al.*, 1996], a high-conductivity layer observed at the same (about 15 to 20 km) depth on INDEPTH MT data [Chen *et al.*, 1996], and a broad midcrustal (20 to 60 km depth) low S wave seismic velocity layer [Kind *et al.*, 1996], are associated with these bright spots. These observations provide evidence that the northern Yadong-Gulu rift is underlain by concentrations of fluids semicontinuously aligned at about 15 km depth at the top of the Tibetan middle crust [Brown *et al.*, 1996; Makovsky *et al.*, 1996; Chen *et al.*, 1996; Kind *et al.*, 1996; Nelson *et al.*, 1996]. Nelson *et al.* [1996] suggest that Tibet is underlain by a midcrustal partial-melt layer, the top of which broadly coincides with the 15-km-deep bright-spot horizon. They interpret the Tibetan bright spots to be magma bodies at the top of this layer. This interpretation requires that minimum-melt temperature (about 650°C [Luth *et al.*, 1964]) is reached at the bright spots, at a depth of about 15 km, which is hard to reconcile with the low temperature inferred for the upper mantle. An alternative interpretation is that the Tibetan bright spots mark concentrations of free aqueous fluids. This interpretation constrains (as discussed below) the temperature at the bright spots from exceeding the wet granite solidus and allows for much lower temperatures (<650°C).

The purpose of this paper is to provide a direct measurement, based on seismic data alone, of the physical properties of the Tibetan bright spots, then based on these measured prop-

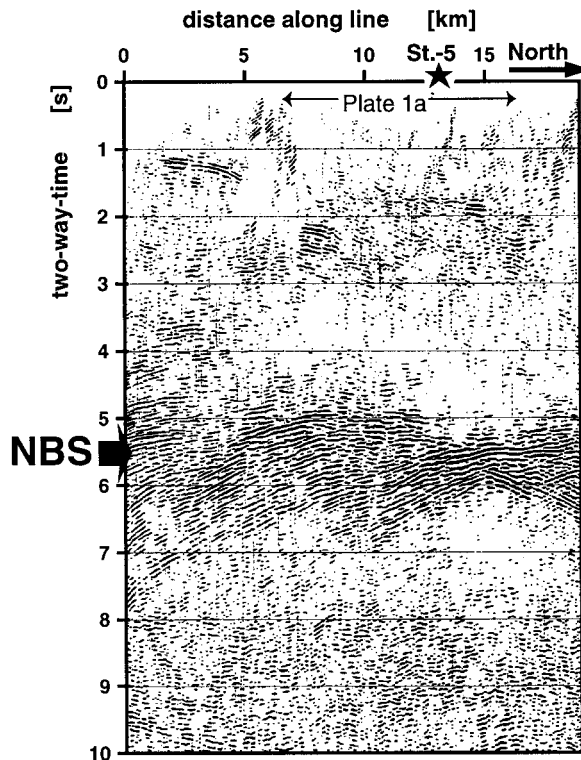


Figure 2b. Enlargement of Tib-9 CMP 15-fold stacked section (unmigrated; from Brown *et al.* [1996]) showing in detail the Nyinzhong bright spots (NBS). Two bright spots are shown at about 5- to 6-s twt within a 2-s twt wide band of reflectivity (arrow). Note geographic region shown in Plate 1a.

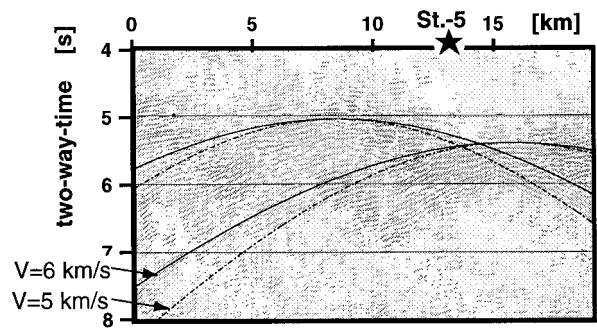


Figure 2c. The 4- to 8-s portion of Figure 2b overlain by diffraction curves for two point diffractors beneath a constant-velocity upper crust with velocities of 5 km s⁻¹ and 6 km s⁻¹. The match with the onset phases of the bright spots' reflective band suggests that the Tibetan bright spots are short segments (diffracting bodies of limited lateral extent), just at the limit of our resolution (about 1 to 2 km).

erties to distinguish between the two alternative models discussed above. First, we provide a qualitative characterization of the bright spots as they appear on our single-fold, three-component, 10- to 20-Hz, wide-angle data. Subsequently, we describe our scheme for measuring and normalizing the full-wave-field-amplitude variation with offset (AVO), and the modeling procedures we used to constrain the range of bright-spot seismic velocities that can produce the measured AVO signature. We describe a wide range of modeling procedures and demonstrate that our results are robust with respect to the various assumptions underlying our measurement and normalization procedures. We conclude by projecting the constrained range of seismic velocities on theoretical rock physics bounds, which suggest that these velocities result from the presence of aqueous fluids at the Tibetan bright spots.

2. Data Acquisition

Our seismic data were acquired in the summer of 1994 as the second phase of project INDEPTH [Nelson *et al.*, 1996; Zhao *et al.*, 1993]. A Ministry of Geology and Mineral Resources (MGMR) of the People's Republic of China seismic crew acquired CMP reflection data along nine profile segments with a total length of about 250 km stretching from the Crystalline Himalaya northward into the Tibetan plateau (Figure 1). Explosive sources, mostly boreholes containing 50- to 200-kg dynamite, were triggered every 200 m along the profile and recorded by a 6-km-long, 240-channel receiver spread. The data were processed to produce 15-fold stacked sections of the line segments [Brown *et al.*, 1996; Alsdorf *et al.*, 1998a, b].

The wide-angle component of project INDEPTH acquired three-component seismic data at a wide range of offsets to provide constraints on the deep structure and composition of the Tibetan crust. This paper focuses on data recorded at six wide-angle stations in the northern Yadong-Gulu rift (Figure 1) north of the YZS. These stations were deployed by a Stanford University-Chinese Academy of Geological Sciences (CAGS) team along INDEPTH CMP segments 6-to-11 (Table 1a; Figure 1) for the 5-month duration of the CMP experiment. Each station was equipped with a REFTEK digital three-component seismograph and a GPS clock that provided precise absolute timing. The INDEPTH explosive sources were recorded at each of the stations by a single, either broadband

a. Station-5: near-vertical incidence

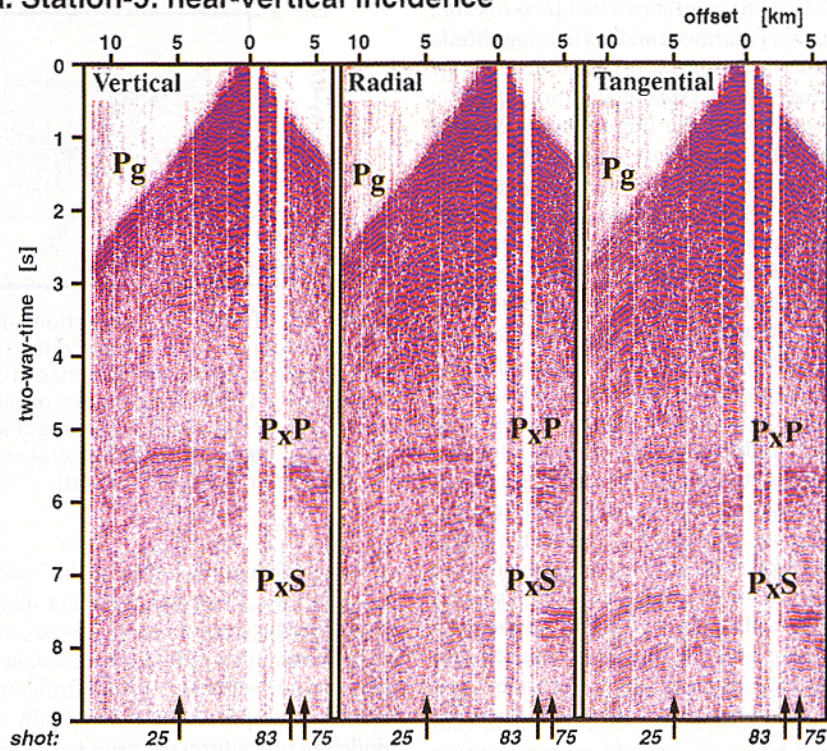
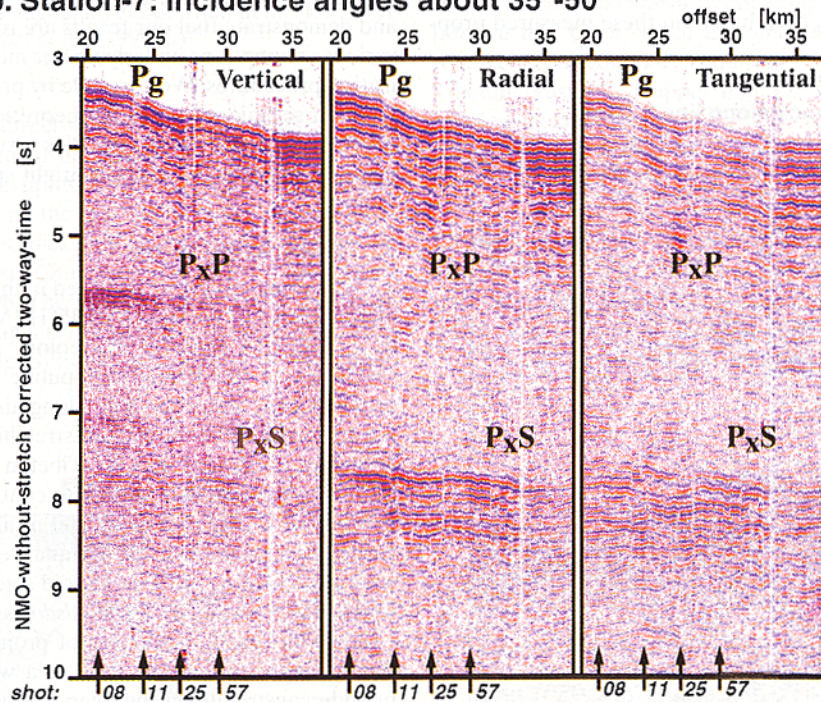
b. Station-7: incidence angles about 35° - 50° 

Plate 1. Typical Tibetan bright spots on INDEPTH wide-angle three-component data: two example receiver gathers (stations 5 and 7 (Table 1b)) formed from the same shots of line Tib-9. Data are bandpass filtered 8 to 36 Hz and plotted trace sequentially with true amplitude and lateral trace equalization. Three panels are displayed for each receiver gather, each panel is an individual component (vertical, radial, and tangential). P_g , direct P wave (P_g); P_{xP} , P_{xS} , phases reflected off the bright spots. Station 7 (Plate 1b) data are time shifted by the twt normal-moveout correction appropriate for a reflector with 5.5-s zero-offset time in a 5.3 km s^{-1} constant velocity crust (NMO without stretch). Compare the sharp (only about 0.2-s duration) bright-spot reflections on the vertical component of station 5 single-fold data with the band of reflectivity on the 15-fold stacked section (Figure 2b). Note the diminution of P_{xP} amplitude at 25- to 35-km offset (Plate 1b). Arrows identify traces used in Figures 3, 4, and 5.

Table 1a. INDEPTH CMP Profiles in the Northern Yadong-Gulu Rift

Line	South End		North End		Number of Sources	Line Length, km
	Longitude	Latitude	Longitude	Latitude		
Tib-6	90°23'E	29°45'N	90°20'E	29°58'N	106	27
Tib-7	90°27'E	29°51'N	90°31'E	30°06'N	137	32
Tib-8	90°25'E	30°04'N	90°29'E	29°60'N	47	10
Tib-9	90°46'E	30°19'N	90°58'E	30°24'N	94	23
Tib-10	90°48'E	30°22'N	90°50'E	30°19'N	26	7
Tib-11	91°04'E	30°28'N	91°22'E	30°34'N	105	36

or midfrequency range, three-component sensor (Table 1b). The data were reduced into receiver (station) gathers (Plate 1) as summarized by *Makovsky and Klemperer* [1996] and are freely available from the IRIS-PASSCAL Data Management Center (<http://www.iris.washington.edu/>).

3. Reflection Character of the Bright Spots

3.1. Reflection Geometry and the Extent of a Bright Spot

The bright-spot P wave reflections, P_xP , appear on the INDEPTH CMP 15-fold stacked sections (Figures 2a, b) as a wide (1 to 2 s twt) band of reflectivity, with local dips up to 30°, at a twt of 5 to 6 s [Brown *et al.*, 1996]. In contrast these P_xP reflections, when seen at near offset on the wide-angle data (Plate 1a), form a series of discrete diffraction hyperbolae, each extending about 10 to 15 km laterally. Examination of the CMP stacked section reveals the same diffraction hyperbolae at the onset of the bright-spot reflections. The curvature of these bright-spot reflection onsets matches the trend of constant-velocity diffraction curves [Sheriff and Geldart, 1995] calculated for point scatterers beneath a constant-velocity layer with a reasonable average upper crustal P wave velocity between 5 and 6 km s⁻¹ (Figure 2c). We suggest that reflective phases following these onsets result from near-surface reverberations (as discussed below). Direct migration of the wide-angle reflection is not appropriate because the data are too sparse and because of the existence of data gaps, while migration of the CMP stacked section is biased by the dips of the reverberatory phases. The bright-spot scatterers are large enough to give rise to distinct reflections; therefore their minimum dimensions exceed the Rayleigh scattering domain [e.g., *Mavko et al.*, 1998] and are constrained by the largest seismic wavelength reflected (about 500 m at 10 Hz). The less than perfect fit of the onset phases to the calculated diffraction curves (Figure 2c), and their sometimes complicated appear-

ance (e.g., at about 5 s between 5 to 10 km along Tib-9, Figure 2b), suggest that a bright spot extends laterally to about the limit of our lateral resolution, given approximately by the width of the first Fresnel zone [Sheriff and Geldart, 1995]

$$(V_p/2) \cdot \sqrt{T/f} \approx 1 \text{ to } 2 \text{ km} \quad (1)$$

where $V_p \approx 5.5 \text{ km s}^{-1}$ is the P velocity above the reflector, $T \approx 5 \text{ s}$ is the reflection twt, and $f \approx 10 \text{ to } 25 \text{ Hz}$ is the frequency range of the reflected wavelet.

3.2. Reflection Amplitude and Composition of the Bright Spots

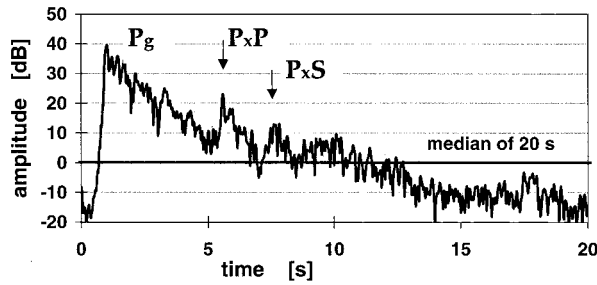
Reflections from bright spots were recorded by the wide-angle stations at offsets of 0 to about 100 km. Data gaps in this coverage result from gaps in the CMP profiles (Table 1a) and from occasional instrumental malfunction of the wide-angle stations (typically, battery failure). The character of these reflections changes considerably with the recording offset. At near-vertical incidence (Plate 1a) the bright spots appear predominantly as 5 to 6 s twt (after normal-moveout (NMO) correction), 10- to 25-Hz, high-amplitude P wave reflections (P_xP). The amplitude of P_xP rises locally up to about 20 dB above background level (Figure 3a), equivalent to the amplitudes measured on the higher-frequency CMP data [Brown *et al.*, 1996]. A. R. Ross *et al.* (Analysis of seismic bright spots in southern Tibet: The case for magma, submitted to *Journal of Geophysical Research*, 1998, hereinafter referred to as submitted manuscript, 1998) estimate the Damzhung (Figure 2a) bright spot's zero-offset P wave reflection coefficient to be about -0.4 ± 0.15 . This estimate, which is corrected for focusing and tuning, suggests a P wave velocity contrast $\geq 40\%$ with about 4% density contrast, and is consistent with the estimate of about -0.6 to -0.3 for the reflection coefficient of the Socorro bright spot which is about 10 dB above background level [Brocher, 1981; Ake and Sanford, 1988]. Note that the

Table 1b. INDEPTH Wide Angle Stations That Recorded the Data Discussed in This Paper

Station	Location		Elevation, m	Sensor Type/Frequency/Sensitivity	Samples s ⁻¹
	Longitude	Latitude			
4	91°01.4'E	30°31.1'N	4660	L28/4.5 Hz/30 V m ⁻¹ s	100
5	90°54.6'E	30°22.8'N	4240	CMG-3T/BB*/2000 V m ⁻¹ s	50
6	90°46.5'E	30°17.8'N	4420	L28/4.5 Hz/30 V m ⁻¹ s	100
7	90°38.9'E	30°13.3'N	4630	L4/1 Hz/171 V m ⁻¹ s	100
8	90°32.9'E	30°07.8'N	4360	CMG-3T/BB*/2000 V m ⁻¹ s	50
10	90°24.8'E	29°59.9'N	4360	CMG-3T/BB*/2000 V m ⁻¹ s	50

BB, broadband; L4 and L28 are Mark-Products sensors; asterisk, CMG-3T is a Guralp sensor with usable frequency range of 0.01 to 30 Hz.

a. Station-5, shot-83, offset 3.4 km (broad-band sensor)



b. Station-7, shot-57, offset 28.6 km (1-Hz sensor)

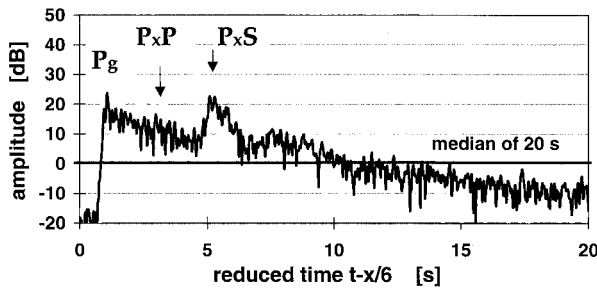


Figure 3. Three-component observed (black curves) seismogram amplitude envelopes (in dB) normalized by the median of the 20-s time window starting approximately at the first-arrival (P_g). Amplitude envelope is the RMS of the complex amplitude of the three components. Also shown (in gray) are equivalent amplitude envelopes for synthetics modeled for offsets of 3.5 and 28.5 km (see discussion about the explicit model in the text and the seismograms in Figure 12a). Arrows mark the onset of P_xP and P_xS reflections from the bright-spots. (a) P_xP is about 20 dB above background at near offset and (b) diminishes at longer offsets. P_xS is weak at near offset but reaches about 20 dB above background at 30- to 40-km offset.

Tibetan bright spots, like many other basement bright spots, are isolated high-amplitude reflections beneath an essentially transparent upper crust (Figure 2 and Plate 1). This, in contrast to most hydrocarbon-reservoir bright spots found within continuously reflective sedimentary basins, suggests that the upper crust above the bright spots, and beneath the shallow (about 1 km deep [Cogan *et al.*, 1998]) northern Yadong-Gulu rift basins, is relatively homogeneous with respect to the wavelength of our data (about 10^2 – 10^3 m). Prominent P to S converted reflections (P_xS) were recorded from the bright spots, predominantly on the horizontal components of our seismometers, at 7 to 8 s twt (after NMO correction) even at near-vertical offsets. The amplitude of P_xP decreases with offset until it essentially disappears at offsets of about 30 to 40 km (Plate 1b), whereas the amplitude of P_xS increases to about 20 dB above background level at offsets of about 30 to 40 km (Figure 3b). This type of AVO for mode-converted reflections (as discussed below) is characteristic of a negative (high over low) velocity contrast at the reflector. The high amplitude of the reflections implies a large reduction in velocity at the top of the bright spots, which in the middle-crust implies the presence of a relatively high volume fraction of fluids at this reflector [Makovsky *et al.*, 1996].

3.3. Reflection Waveform and Internal Structure of the Bright Spots

Brown *et al.* [1996] show a negative reflection polarity for the Tibetan bright spots by comparing the onset of the bright-spot

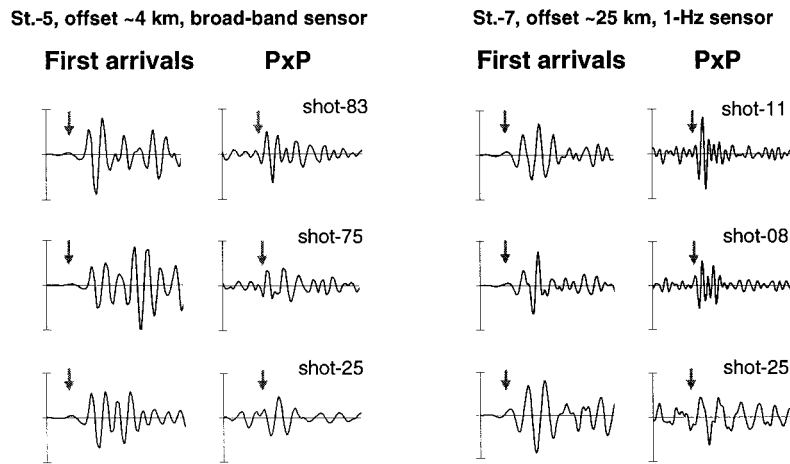
reflections to the polarity of the direct wave. Similar direct determination of the P_xP reflection polarity at wide angle is essentially impossible due to the emergent nature of our data, a result of automatic application of a zero-phase (acausal) anti-alias filter during acquisition by our Reftek seismographs. The P_xP waveform is complex and varies laterally (Figure 4a), which could be interpreted as an indication for internal structure and layering of the bright spots [Ake and Sanford, 1988; Husseiner *et al.*, 1996; A. R. Ross *et al.*, submitted manuscript, 1998]. However, the horizontal particle motion projections of P_xP , as delineated on polar plots (Figure 5), differ significantly between the major phases of the waveform. This variation suggests that the complex waveforms are composed of waves arriving at the station from different directions, as the horizontal particle motion of a P wave incident at the station gives the approximate back-azimuth of its last reflection point. We argue (based on modeling discussed below) that the true P_xP waveform is in acceptable agreement with a single-cycle zero-phase wavelet and that the complexity observed on our data results from superposition of reflections from different bright spots and reverberations near the surface (Figure 3). No additional internal structure is required by our data.

The P_xS phase extends up to 2 s in its duration, and exhibits variable waveforms on the radial and tangential components, which are locally significantly different (Plate 1b). Our attempts to define consistent polarization directions were futile, and S wave splitting, if it exists, is not resolvable (<50 ms). S to P wave converted bright-spot reflections (S_xP) should theoretically arrive at the P_xS twt and be incorporated with this phase. However, S wave reflections from the bright spots (S_xS) are indiscernible on our data, entirely characteristic of data recorded from explosive sources, which leads us to assume that the contribution of S_xP to P_xS is negligible. We suggest, based on reflectivity modeling (discussed below), that the complex appearance of the P_xS phase is a result, as in the case of P_xP , of reflections from different bright spots convolved with reverberations of the downgoing P wave and the upgoing S wave in the shallow basins near the receiver. The low propagation velocity of the upgoing S waves results in the long duration of the P_xS phase. The complexity of the P_xS phase therefore does not necessarily provide evidence for internal structure of the bright spots or for the presence of any significant S wave anisotropy.

4. AVO Analysis of the Tibetan Bright Spots

To obtain the physical properties of the Tibetan bright spots in terms of their elastic moduli M , we analyzed the AVO of the bright-spot reflections. The reflection coefficient B of a wave incident at different angles i on an interface is a function of the contrast of elastic moduli M at the interface and of the geometry of that interface (see Notation for symbols used in this discussion). Our AVO analysis is based on estimating the reflection coefficient of the bright spots as a function of incidence angle $B(i)$ from the amplitudes measured at the surface as a function of offset $A_b(h)$, and then constraining by modeling the range of elastic moduli M that may possibly produce the estimated $B(i)$. AVO analysis is a tool frequently used in hydrocarbon exploration, and many publications discuss the procedures, limitations and potential pitfalls of this technique [e.g., Castagna and Backus, 1993]. The analysis procedure requires the following: (1) a reliable measurement (estimate) of the recorded reflection amplitudes, $A_b(h)$; (2) measuring the

a. Observed waveforms



b. Modeled waveforms, offsets 4 and 5 km, 10-15 Hz zero-phase wavelet

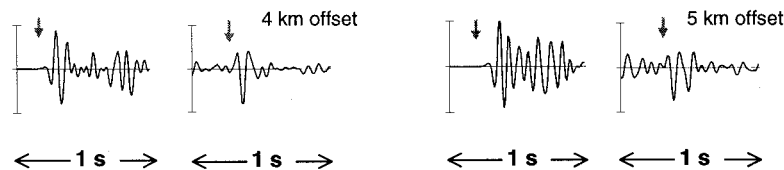


Figure 4. (a) Examples of single-trace P_xP waveforms compared to first arrivals (P_g) in 1-s time windows. Data are band-passed 6 to 36 Hz; amplitudes of the different windows are approximately equalized to each other, but there is no internal scaling within each window. Arrows point to approximate onset of the phases. Note the emergent nature of the arrivals, due to zero-phase anti-alias filtering during acquisition. P_xP waveform is complex and laterally varying in contrast to the consistent waveform of P_g . Full traces are plotted in Plate 1 (arrows). (b) Two examples of synthetic P_xP waveforms and associated first arrivals, displayed as in Figure 4a modeled for 4 and 5 km offset in a single run of the explicit reflectivity model (see text), in which the bright spots are 1 km segments, spaced 5 km apart, and the source is a single-cycle zero-phase wavelet. The double pulse at 5-km offset, which might have been interpreted as internal structure, is a combination of reflections from two adjacent bright spots. Full seismograms are presented in Figure 12a.

amplitude of reflections from a uniform reflector, with adequate sampling over a range of offsets; (3) construction of a seismic velocity model for the crust above the reflector, in order to estimate the elastic moduli above the reflector and the reflection ray path geometry, so as to constrain the angle of incidence as a function of the offset, $i(h)$; (4) derivation of the reflection coefficient B from the recorded amplitude A_b , by correcting the recorded values for all other amplitude contributions along the reflection ray path; and (5) modeling to constrain the elastic moduli and to examine the sensitivity of these parameters with respect to the assumptions made and other sources of error. The particulars of our AVO analysis procedure are as follows.

1. We obtain a robust estimate of the reflected amplitude from the total energy of the full wave field reflected at the bright spots, avoiding the need to confront the complexity of the reflected waveform.

2. We measure the average AVO for a set of reflectors, rather than for a single depth point. This averaging is permitted by the consistency of the amplitudes of reflections from the different bright spots; provides a significant number of measurements over a broad range of offsets; and averages out local effects allowing modeling of the amplitudes in a simplified one-dimensional (1-D) seismic velocity model.

3. We use a data-based correction scheme to derive the bright-spot reflection coefficient from our measured AVO.

This scheme uses the observed data amplitude decay to normalize the measured AVO, and is equivalent to correcting the AVO of the bright spot with respect to the “known” AVO of the random crustal reflectivity.

4. We measure and model the shape of the AVO curve out to “postcritical” angles and do not rely on the absolute values or exact change of the reflection amplitudes as is commonly done in industry. This approach makes our results robust with respect to the internal structure of the bright spots and to upper crustal amplitude losses that are not accounted for in detail by our normalization scheme.

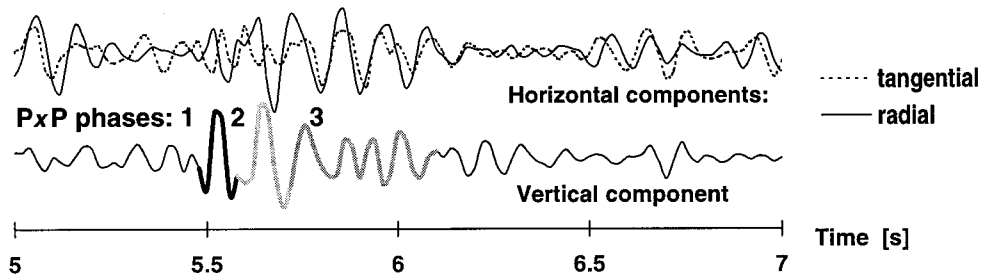
Next we discuss details and tests of our procedure.

4.1. Our AVO-Measurement Scheme

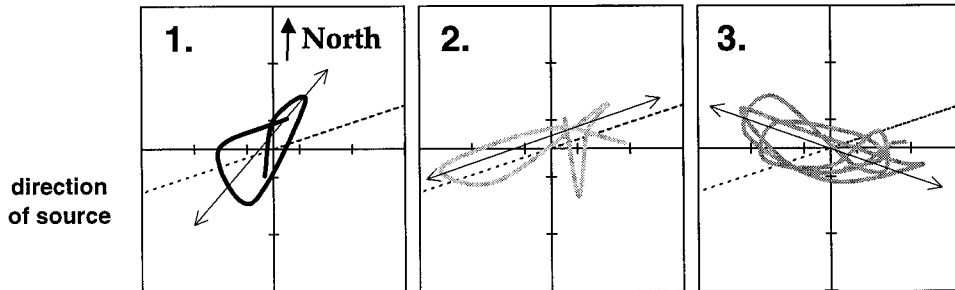
AVO measurement should generally be performed as a function of incidence angle for each individual point on the bright-spot reflector. This approach is not possible for us because of our sparse data coverage, which in turn is a consequence of the serendipitous discovery of these bright spots and the difficulties of acquiring seismic data in Tibet. We obtain an adequate offset coverage for our analysis by assuming that the bright spots imaged along about 150 km of the INDEPTH profile are similar in their properties, then merging all the reflections we recorded off the bright spots into a single “supergather.” This approach is made possible by the homogeneity of crustal basement and tends to average out the effects of

a. Station-5, shot-75, offset 4.3 km:

Three-component displacement seismogram

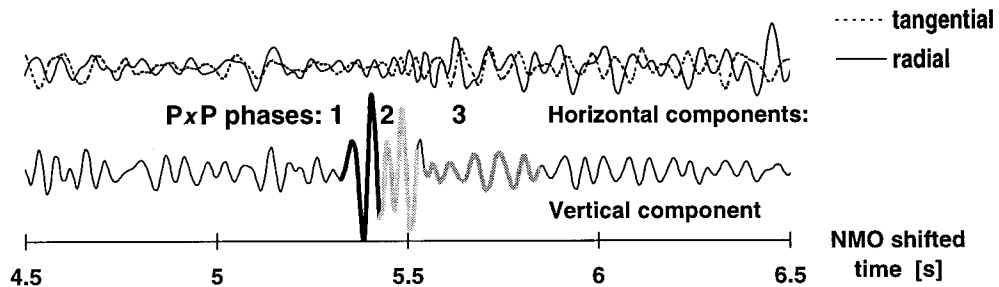


Polar plots of the horizontal components



b. Station-7, shot-08, offset 20.4 km:

Three-component displacement seismogram



Polar plots of the horizontal components

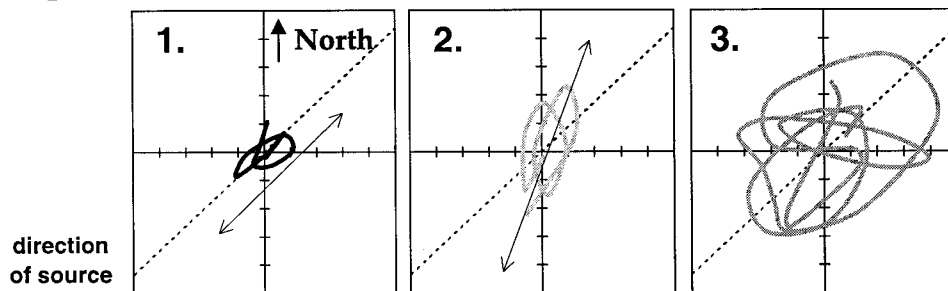


Figure 5. P_xP waveforms and polar plots in the horizontal plane. Each example includes the following: (top) a 2-s time window (encompassing P_xP) of vertical, radial, and tangential particle-motion seismograms; (bottom) three time-sequential polar plots of the horizontal components (map projection of the particle motion) corresponding to P_xP segments as marked and numbered on the vertical component above. All data are plotted true-amplitude. On the polar plots the dotted line marks the source-receiver azimuth and the arrow marks the (interpreted) temporary particle-motion azimuth, interpreted as the P_xP incidence azimuth. In both representative examples (Figures 5a and 5b) the first two time segments have large vertical amplitudes but differ in horizontal azimuth and amplitude: that is, whereas both represent waves incident steeply from below, each arrives from different reflection points. Segment 3 is a reverberative side-reflection incident at low angle, probably from near-surface reverberations in the shallow basins, and may form a substantial part of the reflectivity band on the CMP section (Figures 2a and 2b).

small-scale structure of each individual bright spot. Usually, AVO analysis is limited by the typical hydrocarbon-industry recording parameters to so-called “precritical” amplitude variations at incidence angles up to about 40° [e.g., *Sanford et al.*, 1977] and is limited to P wave recording only. In contrast our AVO analysis is significantly strengthened by the use of the so-called “critical to postcritical” amplitude variations at angles up to 65° (much like the *Pratt et al.* [1993] analysis of the Surrency bright spot), by integration of the amplitude recorded on three components, and by the use of S wave measurements.

The bright-spot reflection has a variable waveform with length of about 1 s twt on our three-component seismogram. To circumvent the complexity of the waveform, we estimate the reflection amplitude as the square root of the reflected energy recorded at the receiver on all three components. In practice, we calculate the RMS of the amplitudes which is equivalent to the mean energy. We define the complex amplitude (amplitude envelope) $A(t)$ of a three-component seismogram, following the definition for the single component case [*Sheriff and Geldart*, 1995], as the sample-by-sample RMS of the three components:

$$A(t) \equiv \sqrt{\frac{1}{3} \sum_{k=1}^3 |a_k(t) \cdot \exp[i \cdot \theta_k(t)]|^2} \quad (2)$$

where a_k and θ_k are the instantaneous trace amplitude and phase respectively of component k ; t is the recording time; i is the complex square root of -1 ; and the absolute-value squared implies a multiplication by the complex conjugate. We then integrate the reflected phase energy, approximating the mean amplitude A_b of a bright-spot-reflected phase as

$$A_b \approx \sqrt{\frac{1}{\Delta t} \sum_{t=T}^{T+\Delta t} A(t)^2} \quad (3)$$

where T is the twt of the reflected phase (e.g., for P_xP at zero offset $T \approx 5$ s); and $\Delta t = 1$ s is the duration of our measurement time window. The reflection amplitude A_b measured in this way is a scalar value that does not depend on exact picking of the reflection phase, or changes in that phase with offset.

4.2. Our Amplitude-Correction Scheme

The AVO of a reflected wave is the integrated result of a series of amplitude-modifying processes affecting the wave along its travel path (e.g., receiver gain, geometrical spreading, attenuation, transmission losses, scattering, etc.), which are different for each trace recorded at the surface. In AVO analysis we are only interested in changes in the bright-spot reflection coefficient $B(M, i)$ from trace to trace, and therefore need to correct for all other amplitude-modifying effects (see Appendix A). This correction is normally done either explicitly, or by comparing the AVO of interest to that of a reflector of known parameters that lies above, and in proximity to, the reflector of interest (e.g., the sea bottom [*Allen and Peddy*, 1993]). In our case the parameters needed for an explicit correction are not well defined [cf. *Pratt et al.*, 1993], and no other clear reflector of known parameters is present (Figure 2 and Plate 1). We therefore correct the AVO of the measured bright-spot reflections $A_b(h)$ using a data-derived factor $\langle A_s \rangle$ estimated for each trace as the median of the complex-amplitude (amplitude envelope) $A(t)$ of source-generated energy. The median $\langle A_s \rangle$ is expected to be proportional to the

background amplitude due to scattered crustal reflectivity of the seismogram $A_s(t)$ (Figure 3) at its characteristic decay time (equivalent to the characteristic decay time of an exponential). Thus our normalization scheme is equivalent to normalization of the measured bright-spot reflection AVO with respect to the AVO of the background crustal reflectivity. The derivation below is a conceptual explanation of the correction procedure that we found to work well for our data (as demonstrated in Appendix A) and not a rigorous theoretical derivation.

The mean amplitude A_b of the bright-spot P-wave reflection with ray parameter p recorded at the two-way-travel-time T by receiver r , from a source S at an offset h , and measured as described above (equation 3), can be approximately expressed as a function of the bright-spot reflection coefficient $B(M, i)$:

$$A_b(s, r, p, T, h) = S(s, p, f) \cdot L(p, T, v, f) \cdot B(M, i) \cdot R(r, p, f) + A_s(s, r, T) \quad (4)$$

where s is the signal generated at the source; L is the path-dependent amplitude loss of the reflected wave (a composite of spherical spreading, attenuation, transmission losses, and scattering); v is the seismic-velocity structure traversed by the wave; f is the center frequency of the reflection; R is the receiver response; A_s is the background amplitude level due to all other seismic phases and to ambient-noise. All the terms in (4) are mean scalar values, modifying the total energy of the reflected wave, thus the dots imply multiplications rather than convolutions, and integration over a range of the ray parameter p is implied. We cannot reliably constrain the parameters needed to extract $B(i)$ from (4) explicitly. However by making several simplifying assumptions, justified by the particulars of our data, we are able to simplify (4) and normalize the measured reflection amplitudes A_b with respect to all the other terms of (4).

We assume that the southern Tibetan upper to middle crust is homogeneous with weak random reflectivity and constant average seismic velocities and attenuation, beneath the shallow low-seismic-velocity Yadong-Gulu rift basins, so that the path-dependent loss L is independent of s and r . These assumptions are justified by the clear dominance of the direct crustal arrivals (P_g and S_g), the scattered P wave crustal reflectivity and the bright-spot reflections (P_xP and P_xS) throughout our seismograms (Plate 1 and Figure 3). Other reflected phases, including S wave crustal reflectivity, have negligible amplitude contributions to our data. The various amplitude losses of the reflected waves in the shallow basins are significant and strongly variable from trace to trace. However these basins are shallow enough to allow these losses to be incorporated into the station S and receiver R terms. Only a limited range of ray parameters p penetrates through these shallow basins to give rise to all the crustal reflections. In addition, integration over a range of ray parameters is implied by our measurement procedure (equation (3)). Thus we neglect the dependence of (4) on the ray parameter p , outside the implicit dependence present in our calculation of the twt T and angle of incidence i from the offset h in a 1-D model. We assume that amplitude losses and scattering due to random crustal reflectivity are constant with time, and we include them in the attenuation term for the reflected waves. In this case the path-dependent loss term of (4) is proportional to spherical spreading and attenuation as a function of the reflection twt; i.e., $L \approx c \cdot L(T)$. The arguments above apply also for the source-generated crustal reflectivity

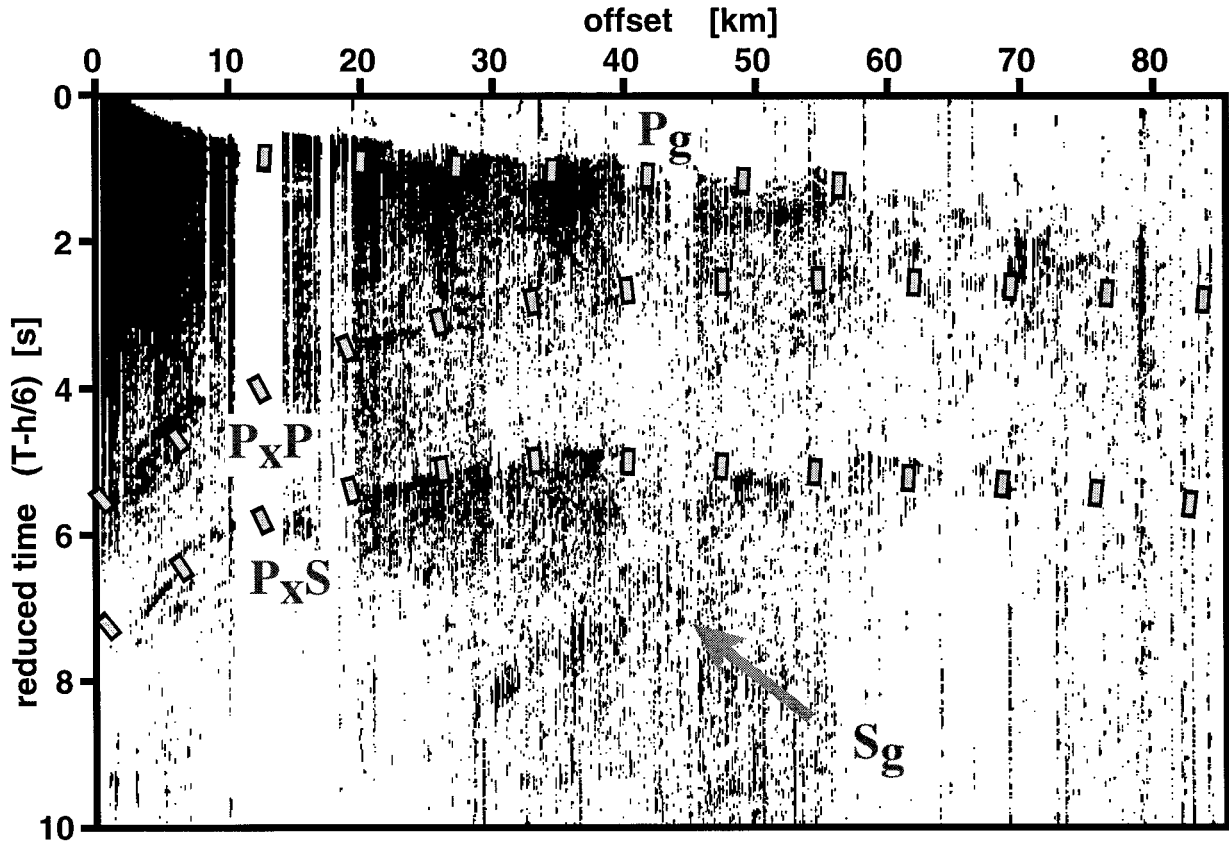


Figure 6a. A 1007-trace subset (the traces with the largest signal-to-noise ratio) of our 2611-trace super-gather plotted in reduced travel time. Each trace is $A(t)/\langle A_s \rangle$, the complex amplitude envelope of three components normalized by the median of the first 20 s of reduced time. The P_xP and P_xS bright-spot reflected phases, although reflected from several different bright spots, appear as coherent and consistent energy bands suggesting that the seismic-velocity structure of the Tibetan crust, down to the bright spots, can be approximated by a 1-D model. (The same coherency is observed with the full data set: a subset of the data was used to produce a clearer image for publication.) Rectangles show predicted travel times of P_xP and P_xS in a constant-velocity model of the upper crust ($V_{P1} = 5.3 \pm 0.2 \text{ km s}^{-1}$, $V_{S1} = 3.2 \pm 0.2 \text{ km s}^{-1}$, $V_{P1}/V_{S1} = 1.65$), and the trend of the direct P wave phase P_g . The direct S wave phase (S_g , gray arrow) crosses the P_xP reflection at 10- to 20-km offset range and the P_xS reflection at 20 to 30 km and distorts amplitude measurements at these offset ranges.

amplitude level, $A_s(t)$, which corresponds to the general amplitude-decay outline of our seismograms (e.g., Figure 3). Averaged over any time window centered at t , A_s can therefore be approximated by

$$A_s(s, r, t) \approx [S(s) \cdot L(t) + N_0] \cdot R(r) \quad (5)$$

where N_0 , the ambient-noise amplitude-level, S and R are assumed to be time independent, and L is averaged over the time window. Note that an average crustal-reflectivity reflection coefficient term (equivalent to B of (4)) is implicit in (5) as part of the scattering which we assume to be constant with time and include in L . Evaluated over a 1-s time window (as in (3)) centered at the bright spot P_xP twt ($t = T$), (5) yields an expression for $A_s(T)$ of (4) as a function of L , S , and R of the same equation 4. Thus evaluating $A_s(T)$ of (5) will allow us to cancel these terms (L , S , and R) from (4) and hence provides the required normalization for (4). We estimate the left-hand side of (5) (A_s) by the median amplitude of the source-generated signal $\langle A_s \rangle$ in the 0- to 20-s reduced-time time window of each trace. This median provides a measure of the time decay rate of the amplitude of the crustal reflectivity

$A_s(t)$ and is essentially not biased by distinct phases, like direct waves and the bright-spot reflections, which constitute amplitude outliers on the seismogram (as demonstrated in Appendix A). The duration over which the median was calculated (the 20-s trace length) was selected to normalize the background reflectivity on most traces to approximately the same amplitude value at the bright-spot reflection twt (Figure 3). Thus assuming that $A_s(s, r, T) \propto \langle A_s \rangle$ (an assumption examined in Appendix A), we divide (4) by (5), neglect the ambient noise in the denominator, and cancel out the (approximately) common factors to obtain

$$A_b(s, r, h)/\langle A_s \rangle \approx c \cdot [B(M, i) + A_s(T)/\langle A_s \rangle] \quad (6)$$

where c is a constant scaling factor, and $A_s/\langle A_s \rangle$ is a constant (≈ 1) of our normalization procedure that expresses the normalized background level. Equation (6) expresses our normalization procedure, and the way we extract our desired parameter B from our observed quantities A_b and $\langle A_s \rangle$. Note that because the scaling factor c is not constrained we cannot calculate the actual value of the reflection amplitudes, and hence

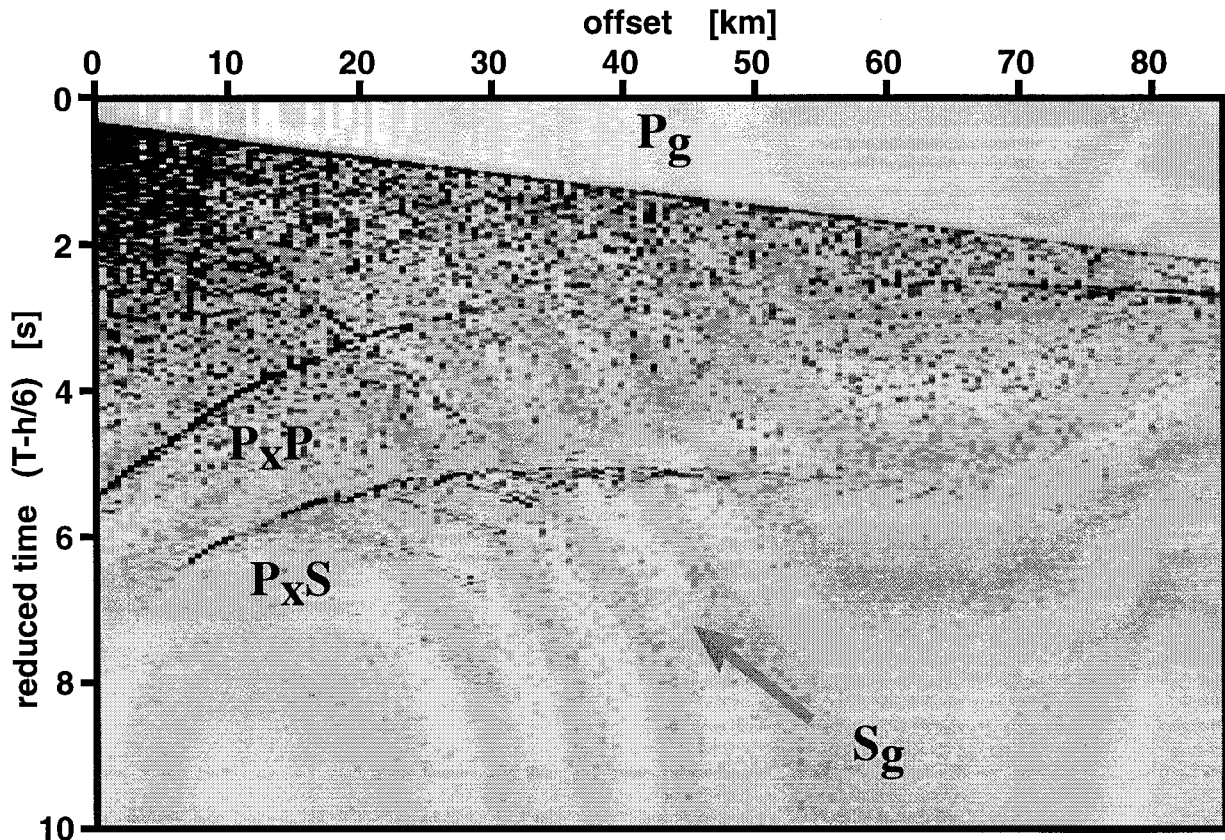


Figure 6b. Synthetic complex amplitude envelope gather generated by explicit reflectivity modeling (see text, and modeled vertical-component seismograms in Figure 12a) and displayed as above. The model has a constant-velocity ($V_{P1} = 5.3 \text{ km s}^{-1}$, $V_{S1} = 3.2 \text{ km s}^{-1}$) crust with random scattered reflectivity, and short (1 km) bright spots, spaced 5 km apart, which have our preferred velocities ($V_{P2} = 3 \text{ km s}^{-1}$, $V_{S2} = 1.6 \text{ km s}^{-1}$).

we restrict our analysis to the relative variation of the amplitudes with offset.

4.3. Our Actual Measurement Procedure and the Measured AVO of the Tibetan Bright Spots

All 2611 three-component seismograms recorded in the northern Yadong-Gulu rift, on wide-angle stations 4, 5, 6, 7, 8, and 10 from source points along CMP line segments Tib 6 to 11 (Figure 1, Tables 1a and 1b), were merged into one supergather. For each seismogram we calculated the true-amplitude envelope (complex amplitude) of each component, using the Hilbert transform. Then for every sample we calculated the RMS of the three components to obtain $A(t)$ of (2). The resulting supergather (Figure 6a) shows, when plotted by offset, the P_xP and P_xS bright-spot reflections as coherent phases, which supports our methodology of merging data from a large area. The data were reduced with a velocity of 6 km s^{-1} , so that the source-generated energy begins within the first 2 s of each trace. The median source-generated signal amplitude, $\langle A_s \rangle$ of (6), was calculated from a 0- to 20-s reduced-time time window. The receiver-gained ambient noise level, $N_0 \cdot R$ of (5), was estimated as the median amplitude of a 60- to 80-s reduced-time time window. The amplitudes of direct P_g and S_g , and of reflected P_xP and P_xS , were obtained from the RMS of 1-s time windows centered at their respective travel-times as measured on our merged supergather (Figure 6a). The 1-s window length was chosen to include the full duration of each phase, and to account for differences in the depth and velocity

of the different bright-spot reflections incorporated into our supergather. The normalized amplitudes of P_xP and P_xS , $A_b(h)/\langle A_s \rangle$, measured from the supergather (Figure 6a), have a bimodal distribution: high values on traces with bright-spot reflections; and low values on traces with only background reflectivity or noise at the travel time of the bright-spot reflections (Figures 7a and 7c). We estimate the normalized background amplitude level at the travel time of the bright spots, $A_s/\langle A_s \rangle$, to be 1.75. We then omit those traces which have a combined RMS normalized amplitude of P_xP and $P_xS < 1.75$, thus limiting our analysis to the 1338 traces (about 50% of the traces) that actually display reflections from the bright spots (Figures 7a and 7c). The amplitudes with values >7 for P_xP (>5 for P_xS) that were measured at offsets of about 10 to 20 km (20 to 30 km for P_xS) (Figure 7a) are biased by the S_g phase which crosses the P_xP (P_xS) phases at those ranges (Figure 6a).

Figure 7a shows that P_xP amplitudes have normalized values of about 4 at offsets up to about 20 km, decrease to about 2 at offsets between 30 and 50 km, then rise again at larger offset. Most of the low-amplitude traces omitted based on combined RMS normalized amplitude <1.75 were recorded at offsets >35 km (Figure 7a). The survival of the obvious minimum in P_xP amplitude after these traces were omitted suggests that this minimum is a robust feature of our data. The P_xS amplitudes are about 2 near zero-offset, rise to about 3 at offsets about 10 to 30 km, then decline again with offset. We tested the variation of these normalized amplitudes, both before and

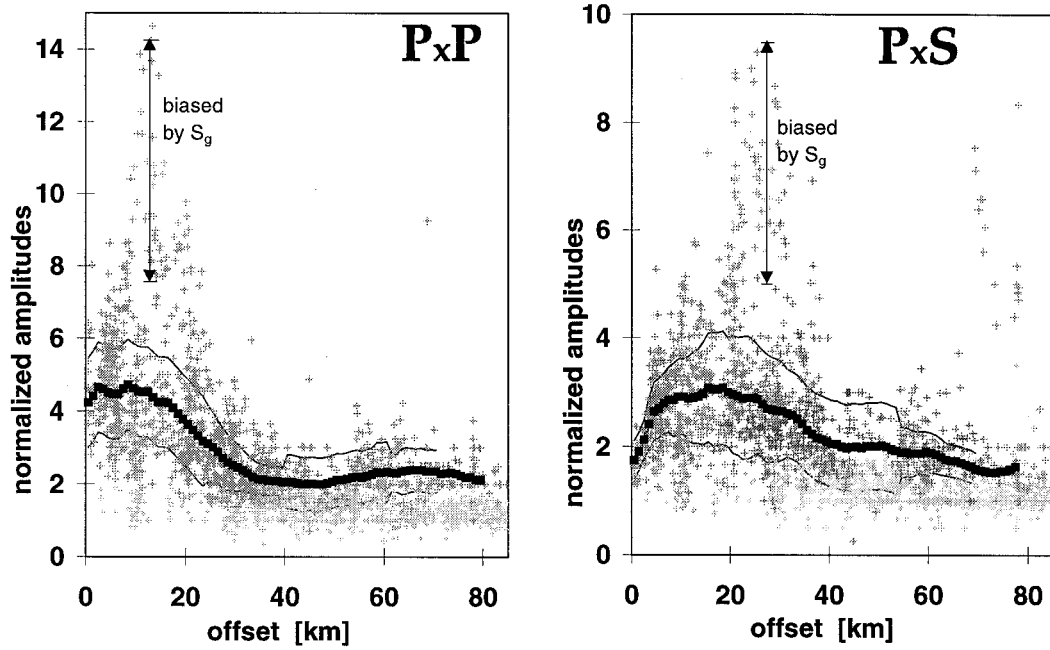


Figure 7a. Normalized amplitudes ($A_b(h)/\langle A_s \rangle$) of equation (6) from the bright-spots supergather (Figure 6a) plotted by offset. Amplitudes are the RMS of 1-s windows centered on the bright spots' travel time; on the left amplitudes measured in the P_xP time window, and on the right P_xS . Dark gray crosses represent traces that were used for our AVO analysis. Light gray crosses represent traces for which the RMS of the normalized P_xP and P_xS is smaller than the average background level of 1.75, that is, traces which show no reflections from the bright spots and were omitted from our AVO analysis. Thick black curve in each plot is the median of the normalized amplitudes in each 1-km bin, smoothed over 10 km; thin curves are error bounds based on the RMS misfit of the data to the smoothed curve. Points with amplitudes >7 (P_xP) or >5 (P_xS) are data biased by the direct S wave (S_g ; see Figure 6).

after omitting traces, and also with respect to source, receiver, and midpoint locations. We found no correlation of amplitudes with respect to source or receiver, which demonstrates the efficiency of our normalization scheme in removing source and receiver effects. In contrast, high P_xP reflection amplitudes are

clearly concentrated at some midpoint latitude ranges (Figure 7c). These regions of high reflection amplitudes correspond to the bright spots imaged by the CMP profiling (YBS, NBS, DBS [Brown *et al.*, 1996]). By omitting the low-reflection-amplitude traces (Figure 7c) we excluded data with midpoints outside of

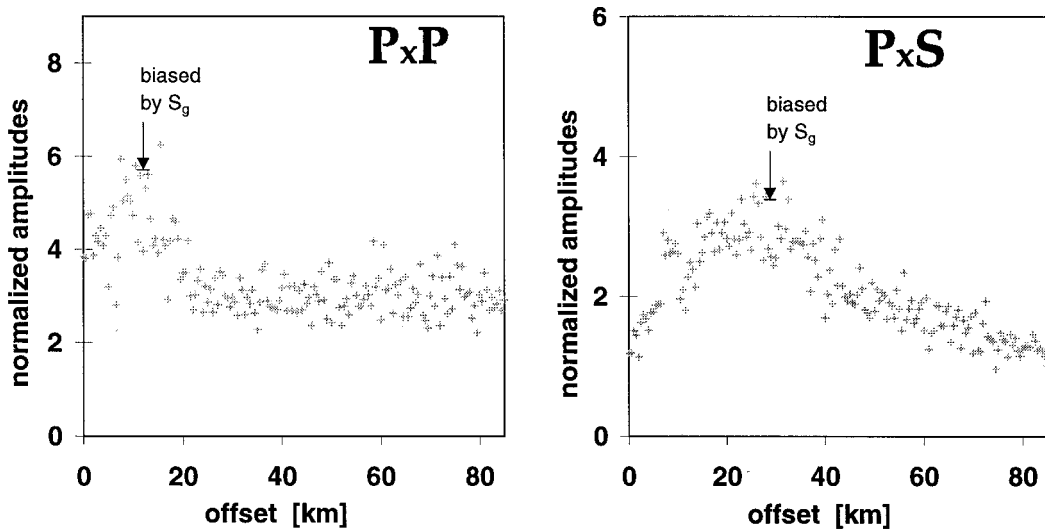


Figure 7b. Normalized synthetic amplitudes measured from the synthetic gather (Figure 6b) generated by explicit reflectivity modeling (see text and Figure 12a) with our preferred bright-spot parameters ($V_{P2} = 3 \text{ km s}^{-1}$, $V_{S2} = 1.6 \text{ km s}^{-1}$). Amplitudes were measured and normalized with the same procedure used for the data. The bias due to S_g is smaller because of the short duration of S_g on the synthetics.

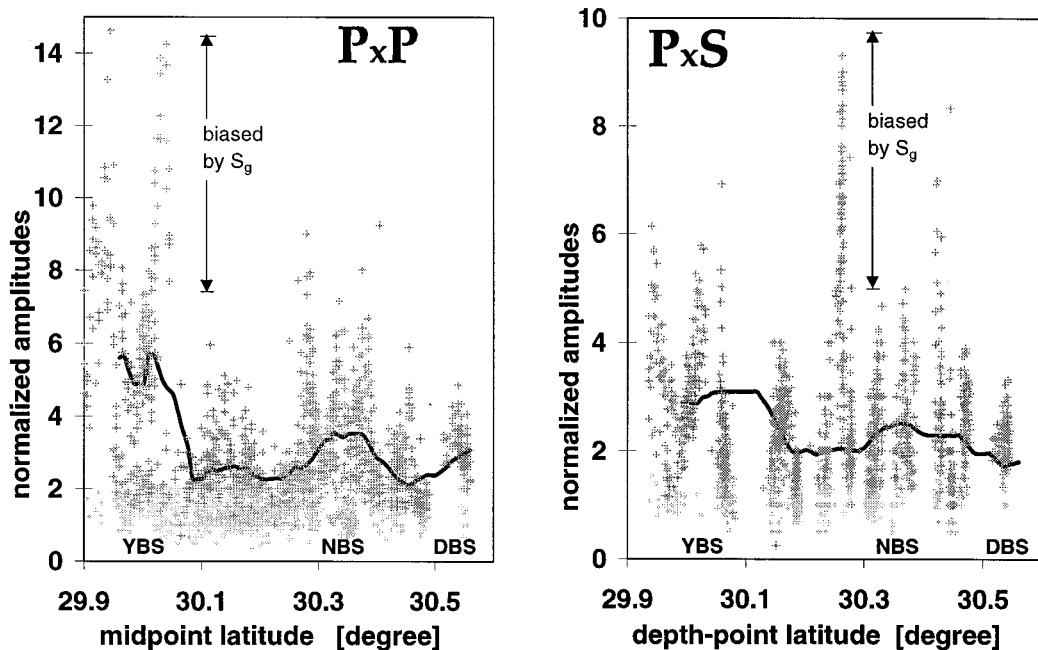


Figure 7c. The same amplitudes as in Figure 7a plotted by reflection depth-point latitude (note that depth points are midpoints for P_xP but not for P_xS). Black curves are binned and smoothed in the same way as the thick curves in Figure 7a. Approximate locations of the bright spots shown in Figure 2a [after *Brown et al.*, 1996] are noted. High reflection amplitudes are correlated with the latitudes of observed bright spots (in the ranges of CMP profiling). Both high and low amplitudes correspond to these latitude ranges, so the correlation of amplitudes with offset visible in Figure 7a is not an artifact of combining reflections from different midpoints.

the high-amplitude ranges and noisy data from our analysis. Thus we made certain that the observed correlation of the amplitudes of P_xP and P_xS with offset is not an artifact of combining reflections from different midpoints. This suggests that defining a single set of elastic parameters to characterize the bright spots beneath the northern Yadong-Gulu rift is a useful approximation.

To allow easier examination of the reflections' AVO we calculated the median of the measured amplitudes in 1-km bins then applied a 50% trim-mean smoothing over 10 km, producing the curves presented in Figure 7a. As a measure of the scatter of the data around these smoothed curves we calculated the RMS misfit of the data to the curve at each bin, and plotted this misfit as error bounds around the smoothed curves of Figure 7a. We corrected this estimate where our measurements are biased by the S_g phase, as discussed above, and where there are only few data points providing only weak constraints for the curves. Thus we manually reduced the error estimate at offsets 5 to 25 km (P_xP) and 10 to 30 km (P_xS); and manually increased the error bounds for P_xP at 45 to 55 km offset. Since the P_xS amplitude at zero offset (i.e., normal incidence) should be zero we estimate the normalized background level of the P_xS time window to be 1.65, approximately the amplitude measured at zero offset. The background level of the P_xP time window is expected to be higher as this phase arrives at earlier travel time, with higher background scattered energy. We estimate the normalized background level of the P_xP time window to be 1.85, which is consistent with the lowest amplitudes measured at about 55 km offset, yielding the combined RMS for both phases of 1.75 used above to recognize and omit data without bright-spot reflections. This estimate is

somewhat arbitrary, but it has negligible effect on our modeling results (see below).

5. Fitting the AVO of the Tibetan Bright Spots

The P_xP and P_xS reflected phases appear on our merged supergather as coherent energy bands with consistent travel times, although they reflect from different bright spots (Figure 6a). This suggests that the average seismic velocity structure of the Tibetan crust, down to the bright spots, has only minor lateral variation. Moreover, the normalized reflection amplitudes are consistent between the different traces (Figures 6a and 7a), suggesting that the different bright spots have similar seismic character. We therefore match the shape of the AVO curves $A_b(h)/\langle A_s \rangle$ (Figure 7a) measured from our merged supergather to the shape of curves modeled using a single set of elastic parameters M for the bright spots and for the crust above them, a 1-D model. We first estimate the velocities of the upper crust from travel time modeling, then use the measured AVO to constrain the parameters of the bright spots. We describe here results of the simplest model (given by the Zoeppritz equations), then show that essentially the same results are obtained from 1-D elastic modeling with increasing levels of complexity. The different models considered here are used to examine the importance of the different assumptions we made in our measurement and correction schemes. Note that while the more complex models may produce results that better resemble the data they also embed additional sets of assumptions. The similarity of all our modeling results suggests that our simple 1-D model, although a gross approximation,

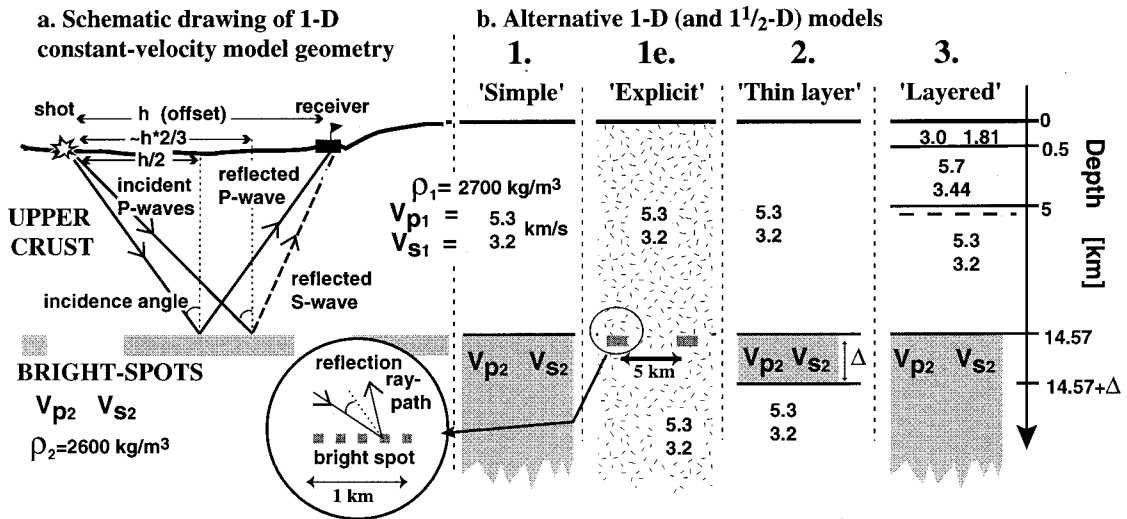


Figure 8. (a) Schematic drawing of P_xP and P_xS ray paths and incidence angles in a constant-velocity model. (b) The parameters of 1- and $1\frac{1}{2}$ -D models used in our modeling of the bright spots: the “simple” model (1)—constant-velocity upper-crustal layer above a half-space bright spot (gray); the explicit model (1e)—a horizon of 1-km bright-spot segments (gray), spaced 5 km apart, embedded in a constant velocity (and attenuation) crust with random scattering (random pattern); the “thin-layer” model (2)—thin-layer bright spot (gray) of thickness Δ in a constant velocity crust; the “layered” model (3)—layered upper crust above a half-space bright spot (dashed line at 5.5 km represents a velocity gradient). The depth to interfaces, and the values of V_p , V_s , and density (ρ), are noted for each layer. An enlargement of a bright spot in the explicit model (circle) shows that each bright spot is composed of several point diffractors (gray), each reflecting the waves independently. The incidence angle is calculated in the explicit model from the angle made between the incident and reflected rays.

provides useful information about the nature of the bright spots.

5.1. Constant-Velocity Travel Time Modeling of the Upper Crust

We model the Tibetan upper crust above the bright spots as a single layer with uniform elastic properties, P wave velocity V_{p1} , S wave velocity V_{s1} , and density ρ_1 , above a horizontal bright-spot reflector (Figure 8a). In this model the ray paths of the reflected phases are straight lines, and the calculation of travel times and angles of incidence and reflection of these phases as a function of recording offset is straightforward. We estimate a depth of 14.57 ± 1.5 km for the bright spots, V_{p1} of 5.3 ± 0.2 km s $^{-1}$, and V_{s1} of 3.2 ± 0.2 km s $^{-1}$ by fitting P_xP and P_xS travel times with calculated travel time curves (Figure 6a). The lack of strong reflectivity rules out the possibility of large-velocity changes above the bright spots (Figure 2 and Plate 1) except at very shallow levels of the crust. This, together with more detailed analysis of the velocity structure in the Tibetan upper crust (see section about elastic modeling below), leads us to suggest that these average velocities reflect, within our error bounds, the actual interval velocities right above the bright spots. Using these velocity estimates, we calculate the incidence and reflection angles (Figure 8a) and plot our “ $B(i)$ curves,” the measured amplitudes as a function of the down-going P wave incidence angle (Figure 9). Ray tracing through various models with a reasonable range of upper crustal velocity structures (including the consideration of gradual velocity changes) suggests that our errors in calculating the incidence and reflection angles are probably $\pm 5^\circ$ at 65° , and significantly less at lower incidence angles. Note that as required by Snell’s law, P_xP and P_xS recorded at the same offset have significantly

different incidence angles, and hence significantly different ray paths (Figure 8a). This fact limits the value of comparing the P_xP and P_xS amplitudes on a trace-by-trace basis as was done by *Makovsky et al.* [1996] and calls for comparison of amplitudes recorded on different traces as is done in this paper.

5.2. Forward Modeling of the Bright Spots: Outline of the Modeling Procedure

To obtain the elastic moduli M characterizing the bright-spot reflecting interface, we forward model our AVO. We calculate the AVO expected for a P wave reflected and converted at the interface for all plausible values of M and compare this calculated AVO to the AVO curves binned and smoothed from our data (Figure 10). Our measure of goodness of fit is the RMS misfit between the modeled and measured curves normalized by our estimated RMS misfit of the data to the smooth curves (Figure 9), calculated at 1° increments between 10° to 65° incidence angles. A constant scaling factor, c of (6), needs to be applied to the measured AVO curves before comparing them to the modeled curves. This scaling factor, approximately the zero-offset path-dependent term of (4), is usually evaluated from the zero-offset reflection coefficient of the bright-spot reflector [Shuey, 1985], which is not well constrained by our data. Therefore we only fit the shapes of the modeled and calculated AVO curves by empirically scaling them to each other. The scaling factor is determined so that it “fixes” the measured and calculated P_xP curves to each other at either 15° or 30° incidence angle. For each set of elastic parameters we examine the fit between the calculated curves twice: (1) when they are fixed at 15° (which effectively fits the ratio of maximum and minimum of the P_xP curve) and (2) when they are fixed at 30° (which fits the slope of the P_xP curve

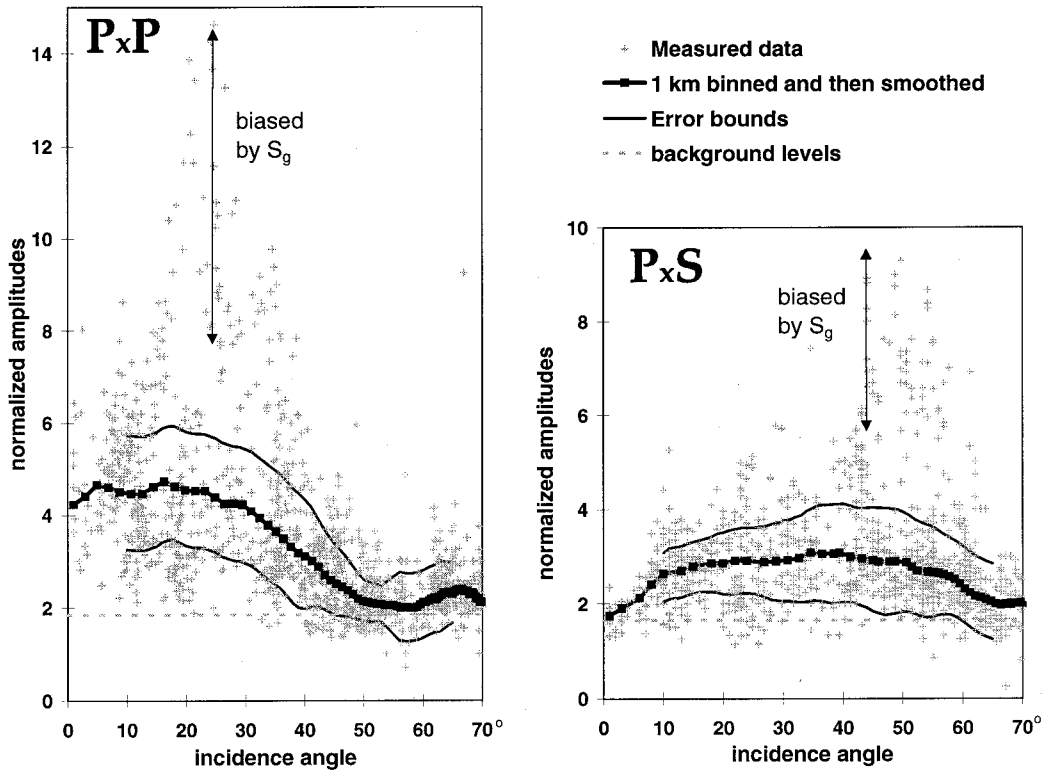


Figure 9. Amplitudes of the bright-spot supergather (as in Figure 7a) plotted as a function of incidence angle calculated using our 1-D constant-velocity model (Figure 8a). Black curves are binned and smoothed medians and thin curves are error bounds (calculated as in Figure 7a). Error bounds are only plotted for incidence angles of 10° to 65°, the range in which they are used to constrain our modeling. Note the most robust feature of the P_xP curves, the amplitude minimum at incidence angle of $55^\circ \pm 5^\circ$. Horizontal dashed lines at 1.85 for P_xP , and 1.65 for P_xS , mark the estimated background amplitude levels.

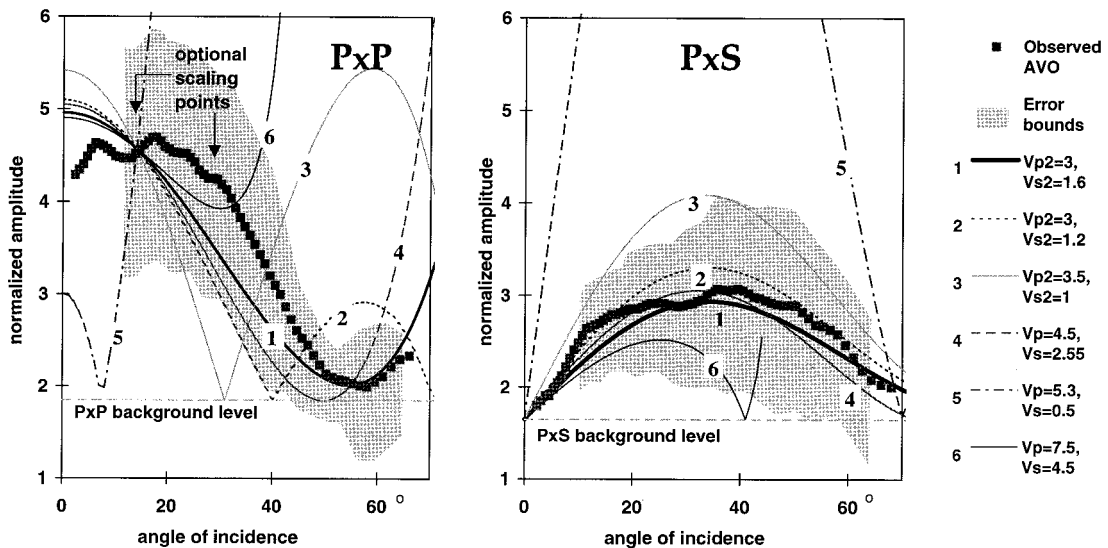


Figure 10. Examples of Zoeppritz-modeled absolute-value amplitude-variation-with-incidence-angle curves for six different bright-spot P and S velocities (listed on right), corresponding to the numbered circles in Figure 11, compared to our binned and smoothed data curves (dark squares) and their error bounds (gray shading). (left) Measured and modeled P_xP amplitude curves; right: P_xS curves. The relative scaling between the data and modeled curves (which cannot be determined by our data) is determined by fixing them to each other at 15° incidence angle. The bright spots are constrained to have low velocities (curves 1 to 4) by the relative P_xP to P_xS amplitudes, while the P_xP curve, in particular the diminished amplitudes at $55^\circ \pm 5^\circ$ incidence angle, shows model 1 to be significantly better than models 2, 3, and 4.

Table 2. Rock and Fluid Points at About 15 km Depth

Material (Rocks and Fluids)	V_{p_1} , km s ⁻¹	V_{s_1} , km s ⁻¹	ρ_1 , kg m ⁻³
Our estimate for the upper layer	5.3	3.2	2700
Granite ^a	6.15	3.5	2630
Melt (andesitic) ^b	2.5	0	2400
H ₂ O ^c	1.55	0	760

Table modified from *Watanabe* [1993].

^a*Bowers* [1995].

^b*Murase and McBirney* [1973].

^c*Fielitz* [1971].

from 30° to 50°). The RMS misfit of the measured and calculated AVO curves is calculated in both cases, and the scaling factor that produces the lower misfit is chosen. This same scaling factor is also applied to the P_xS curve.

The inspection of AVO curves, modeled with several sets of elastic parameters (numbers 1–6, Figure 10), reveals that the shape of our measured P_xS AVO curve constrains our analysis to the class of models with high above low P wave velocity (i.e., negative reflection coefficient) but is then matched by most models in this class. In contrast, the shape of the measured P_xP AVO curve, for which the approximation of (6) is also better defined, is much more indicative of the specific elastic parameters required (Figure 10). In fact, the most indicative feature of the P_xP AVO curve is the incidence angle, 55° ± 5°, at which this curve reaches its minimum. This feature is a robust feature of our data; it is emphasized by the high P_xS amplitudes at the same range of incidence angles (Figure 9), and offsets (Figures 6a and 7a), and therefore it does not depend on our normalization scheme (equation (6)).

The modeled AVO curves were obtained by several methods, presented below in order of increasing complexity and embedded assumptions. In this section we discuss modeling using the Zoeppritz equations; in the following section (Synthetic-Seismogram Modeling of the Tibetan Bright Spots) we discuss methods using synthetics calculated first by the reflectivity method, then as solutions to the elastic wave equation.

5.3. Modeling the Bright Spots by Zoeppritz Equations: The Simple Model

The amplitude change with incidence angle for an infinite-frequency plane-wave reflected at a 1-D planar interface can be calculated explicitly for a set of elastic moduli M using the Zoeppritz equations [*Aki and Richards*, 1980]. The explicit analytical formulation of the Zoeppritz equations provides a computationally fast way to examine the relative effect of the various elastic parameters. However, this formulation provides only the contribution of a single planar interface between two constant-velocity layers. In our modeling we used upper crust parameters $V_{p1} = 5.3$ km s⁻¹, $V_{s1} = 3.2$ km s⁻¹, and $\rho_1 = 2700$ kg m⁻³. We searched for acceptable bright-spot elastic properties beneath the interface by varying V_{p2} from 0 to 7.5 km s⁻¹, V_{s2} from 0 to 4.5 km s⁻¹ in 0.1 km s⁻¹ steps, and density ρ_2 from 1500 to 3500 kg m⁻³. This modeling showed that the density ρ_2 affects only the scale and not the shape of the AVO curves and therefore cannot be constrained by our analysis. We therefore fix the density beneath the interface ρ_2 at 2600 kg m⁻³ in all subsequent analysis. It must be emphasized that

using this density does not affect the results of our analysis, although this density is approximately that of a typical crustal rock saturated with about 5% H₂O or a minimum of 30% melt (Table 2).

The most basic way of examining the match of modeled P_xP curves (Figure 10) with our data is by comparing contours of the lowest angle at which the absolute value of a modeled curve reaches a minimum (there may be more than one such minimum, for example, when a modeled curve changes its sign twice as the angle of incidence increases), with the angle at which the measured P_xP amplitude reaches its minimum (Figure 11a). Inspection of the contour plot (Figure 11a) reveals that only a narrow range of bright-spot velocities produces curves with the first minimum at angles higher than 50°. Moreover, the more reasonable of these velocities (with $V_p > 1.5$ km s⁻¹) suggest a minimal to no change in Poisson's ratio between the upper crust and the bright spots.

A more quantitative way of examining the fit of the modeled curves to the data is to plot contours of normalized model misfit as a function of the velocities V_{p2} and V_{s2} (for the fixed density ρ_2) beneath the interface (Figure 11b). Visual inspection of modeled curves (Figure 10) reveals that only parameter sets with normalized misfit ≤ 0.5 (in the dark gray area of Figure 11b; curve 1 (but not curves 2 to 6) in Figure 10) fit the observed AVO reasonably and should be considered as representing possible parameters of the Tibetan bright spots. Comparison of the contour plots of Figures 11a and 11b shows that the feature of the data that controls our modeling results is the minimum in the measured P_xP AVO curve between 50° and 60° incidence angle, which is the most robust feature of our data (Figure 9). Our results are therefore not much affected either by the scaling of the measured AVO curves or by the bias of these curves by the S_g phase. The general shape of our observed AVO curves (Figure 10; curve 1) are reasonably well fit by the simple modeling procedure of the Zoeppritz equations. However, the curves obtained by this procedure do not match the flattening of the observed P_xP curve at angles below 20° or the vanishing of the observed amplitudes at angles larger than 70°.

In the above modeling, we fixed the velocities above the interface, V_{p1} and V_{s1} (Figure 8b(1)), based on the upper crustal velocities constrained by travel time modeling of the P_xP and P_xS reflected phases and additional data (see section about elastic modeling below). However, these velocities are only an estimate of the interval velocities immediately above the bright-spot reflector. To examine the sensitivity of our results to potential errors in this estimate, we modeled the family of curves resulting by varying V_{p1} by ±0.3 km s⁻¹ (–0.3, 0, and +0.3 km s⁻¹) and V_{s1} by ±0.2 km s⁻¹ (–0.2, 0, and +0.2 km s⁻¹) for each pair of velocities V_{p2} and V_{s2} in the ranges described above. The normalized RMS misfit to our observed AVO for each of the nine resulting curves was calculated, and the best fitting curve was selected. These values are contoured in Figure 11c. Comparison of the ≤ 0.5 range (dark shading) in Figure 11c with that in Figure 11b shows the model sensitivity to the exact velocities above the bright spots and represents an extreme measure of error in determining the range of possible parameters of the bright spots. Our uncertainty in the velocities above the interface essentially maps to an uncertainty of ±0.7 km s⁻¹ in any of the V_{s2} values constrained in Figure 11b but does not change the general trend of best fitting models.

The ≤ 0.7 RMS misfit contour represents an error estimate for our range of probable parameters of the bright spots.

6. Synthetic-Seismogram Modeling of the Tibetan Bright Spots

6.1. Explicit Reflectivity Modeling in 1¹-D

To gain an intuitive feel and make a qualitative test for the validity of our AVO analysis, we generate “realistic” synthetic seismograms based on our basic assumptions. We model the southern Tibetan crust as a homogenous half-space with the constant seismic velocities and density used above, and weak random reflectivity. The bright spots are modeled as a horizontal series of equally spaced short segments, each composed of a series of horizontally aligned, equally spaced, diffraction points. Each diffraction point independently reflects the down-going P wave, as a function of its incidence angle (Figure 8b, “explicit” model). This is labeled “1e” in Figure 8b to make clear the relationship to the Zoeppritz curve fitting (Figure 8b(1) discussed in the previous section: both there and here we calculate amplitudes directly from the Zoeppritz equations assuming a reflective half-space. For simplicity, we ignore in model 1e the thickness of the bright spots (to be discussed later) and the width of the diffraction points composing them. An intuitive and computationally affordable approach to compute “realistic” synthetic seismograms is to sum the reflectivity series of each seismic phase explicitly, then convolve the resulting reflectivity series with an assumed source wavelet. In this model we include the contributions of the crustal direct phases (P_g, S_g), the scattered P wave crustal reflectivity, and the bright-spot P wave, and P to S wave converted, reflections (P_xP, P_xS). The contribution of all other phases (e.g., S wave reflectivity, etc.) is neglected. Thus the vertical component reflectivity ψ_z as a function of time t and offset h is calculated by

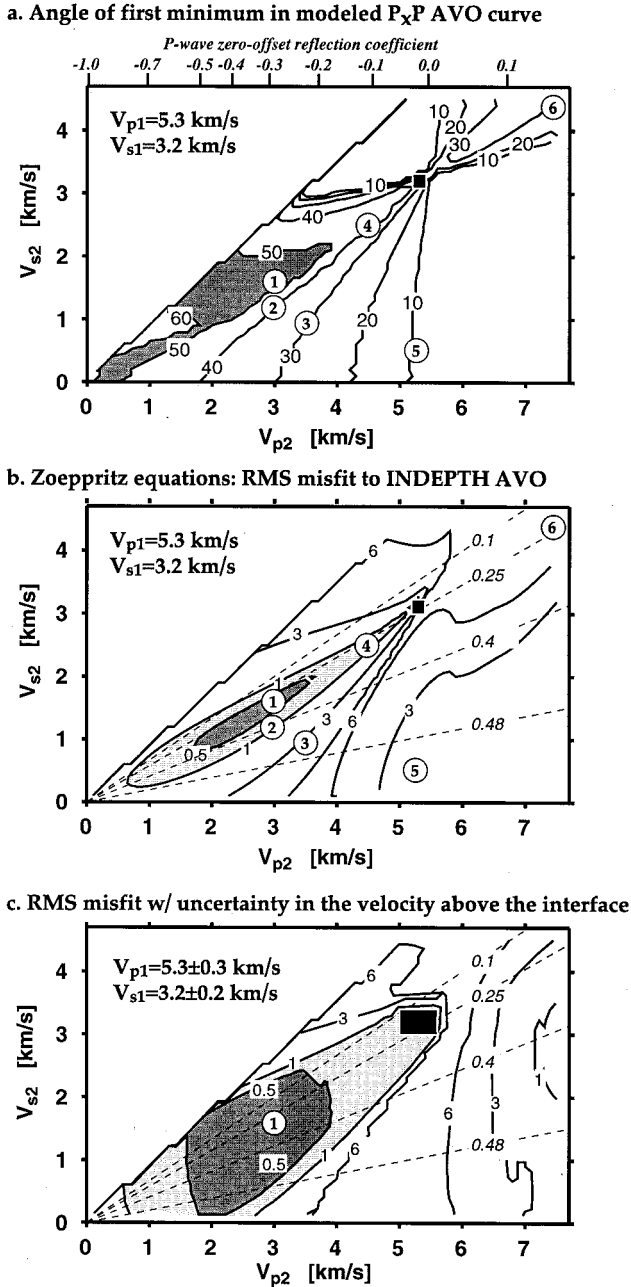


Figure 11. (Opposite) Results of Zoeppritz modeling of the Tibetan bright spots assuming a constant-velocity upper crust above a half-space bright spot (Figure 8b, model 1). Black square represents the upper crust parameters: $V_{p1} = 5.3$ km s^{-1} , $V_{s1} = 3.2$ km s^{-1} , $\rho_1 = 2700$ kg m^{-3} . Results are plotted versus V_{p2} and V_{s2} of the bright-spot half-space (Figure 8b), with the bright-spot density fixed at 2600 kg m^{-3} . Dashed lines in Figures 11b and 11c correspond to constant Poisson ratios. Numbered circles correspond to modeled curves in Figure 10. Circle 1 ($V_p = 3$ km s^{-1} , $V_s = 1.6$ km s^{-1}) represents our preferred parameters for the Tibetan bright spots. (a) Contours of the angle at which the modeled P_xP AVO curves reach a minimum. Gray shading is the range of bright-spot velocities that produces P_xP AVO curves with the minimum at incidence angles between 50° and 60° , in agreement with our observed P_xP AVO curve. The values of the P wave zero-offset reflection coefficient in our model (with $\rho_2 = 2600$ kg m^{-3}) are noted on the top axis. (b) Contours of RMS misfits between the modeled P_xP AVO curves and our data normalized by the error bounds (Figure 9). Gray shading marks the range of parameters with misfit ≤ 1 (light) and ≤ 0.5 (dark): the range of bright-spot parameters that best matches our observations is marked by the ≤ 0.5 range. (c) Contours of normalized RMS misfit, as in Figure 11c obtained by accounting in our modeling for ± 0.3 km s^{-1} and ± 0.2 km s^{-1} error bounds (size of the black square) in the determination of P and S wave velocities immediately above the bright spots, respectively (see text).

$$\begin{aligned}
\psi_z(t, h) = & \delta(t - T_{P_g}) \cdot L(T_{P_g}) \cdot \phi_P + \delta(t - T_{S_g}) L(T_{S_g}) \cdot \phi_S \\
& + H(t - T_{P_g}) B_{cr} \text{rand}(t) L(t) \phi_P \\
& + H(t - T_{S_g}) B_{cr} \text{rand}(t) L(t) \phi_S \\
& + \sum_j \sum_k [\delta(t - T_{P_xP}^{j,k}) B_{PP}(i_{PP}^{j,k}) L(T_{P_xP}^{j,k}) \phi_P \\
& + \delta(t - T_{P_xS}^{j,k}) B_{PS}(i_{PS}^{j,k}) L(T_{P_xS}^{j,k}) \phi_S] \quad (7)
\end{aligned}$$

where

$$L(t) = t^{-1} \exp[-\pi f(t/Q)] \quad (8)$$

is the path-dependent loss due to spherical spreading and attenuation here calculated for frequency $f = 10$ Hz and attenuation quality factor $Q = 200$. The first two terms in (7) produce crustal direct P wave (P_g) and S wave (S_g) respectively, the next two terms produce random P wave and S wave crustal reflectivity, and the last term sums over the P wave reflections (P_xP) and P-to-S wave converted reflections (P_xS) from the different diffraction points of the different bright spots. The $\delta(t)$ value is the delta function, $H(t)$ is the step (Heavyside) function (see appendix for nomenclature); $\text{rand}(t)$ returns a random number in the range $[-1, 1]$; T_{P_g} and T_{S_g} are the arrival times at offset h of the direct P and S waves, respectively; $T_{P_xP}^{j,k}$ and $T_{P_xS}^{j,k}$ are the two-way travel time of a P wave reflection and a P to S converted wave from the k th point of the j th bright spot; $i_{PP}^{j,k}$ and $i_{PS}^{j,k}$ are the angles of incidence of the downgoing P wave producing the bright-spot P wave reflection and P to S converted wave. These angles were determined from the angle between the incident and reflected rays for each diffraction point. The projections to vertical component of the P wave ϕ_P and S wave ϕ_S arrivals were arbitrarily set at $2/3$ and $1/3$, respectively, for the direct waves and the crustal reflectivity and were calculated from the angle of arrival for the bright-spot reflections. The maximum reflection coefficient of the crustal reflectivity B_{cr} was set at 0.1, thus producing random reflectivity in the range $[-0.1, 0.1]$. The bright-spot reflection coefficients of the P wave B_{PP} reflections and P to S converted wave B_{PS} are discussed below. The amplitude a_z of the vertical component seismogram as a function of offset and time is then calculated by

$$a_z(t, h) = \psi_z(t, h) * S + N_0 \text{rand}(t, h) \quad (9)$$

where S is a zero-phase source wavelet with 10- to 15-Hz frequency band; N_0 is the ambient noise level set at 10^{-4} ; and the asterisk signifies convolution. The horizontal component reflectivity series and seismogram are calculated by the same approach of (7) and (9). Note that we neglect here possible differences in the frequency of the different phases or in S wave attenuation and any response due to variations in source or receiver or due to the shallow basins.

Synthetic seismograms that match our data are obtained when we model the bright spots as a series of segments, each segment spaced 5 km laterally, 1 km wide and made up of 5 diffraction points (Figure 8b (explicit)). We calculate the reflection coefficient at each diffraction point using the Zoepritz equations with the bright-spot velocities of curve 1 ("best") in Figures 10 and 11. The resemblance of the modeled vertical seismograms (Figure 12a) to the data (Figure 2 and Plate 1) as further demonstrated by amplitude plots of two of our modeled seismograms (Figure 3) additionally corroborates the validity of our simple model and our choice of modeling

parameters. The complex reflection pattern of both P_xP and P_xS is also duplicated by our explicit model, a similarity which is further demonstrated by comparisons of P_g and P_xP waveforms on two of the modeled seismograms (Figure 4). These results are consistent with our suggestions that the bright spots are a series of short diffracting segments rather than a single reflector, and that no internal structure is required by the data. We calculate the complex amplitude (envelope) of the modeled vertical and horizontal components using the Hilbert transform, normalize the traces by the median of 0- to 20-s reduced-time time window (exactly as done with the data; see Appendix A for discussion), and compare the result (Figure 6b) to our data supergather (Figure 6a). The observed and modeled gathers show a good match in their general features and their offset dependence. All phases are longer in duration on the observed supergather and are fit better when we use a longer-duration source wavelet. Modeling (below) demonstrates that the longer-duration wavelet is generated by reverberations in the shallow basins. Note the good match in the P_xP and P_xS travel times yet poor match of the P_g phase. The observed P_g shows lower than the average (modeled) velocity at the shallow basins and higher than average below that (see discussion below). The bright-spot reflection amplitudes were measured as the RMS of a 1-s time window centered at the modeled travel times (as for the data). Comparing the normalized model amplitudes (Figure 7b) to the normalized observed amplitudes (Figure 7a) shows a good agreement. The biases due to S_g are less pronounced in the modeled amplitudes due to the short duration of this phase in the model, in contrast to its long duration and low-frequency content in the data.

To produce a statistically meaningful contour plot of the misfit between measured and modeled amplitudes (as done above, Figure 11) would be computationally too costly for our explicit model because of the large random constituents of the model. However, a useful qualitative evaluation of the validity of the contour plots in Figure 11 can be obtained from a visual comparison of the measured amplitudes with amplitudes modeled with different bright-spot velocities (Figure 13, curves 1 to 6). This comparison demonstrates that our normalizing factor $\langle A_s \rangle$ (equation (6)) is not sensitive to the bright spots' AVO (see discussion in Appendix B), and that even amplitude curves modeled with bright-spot velocities in the range of misfit >0.5 and <1 (e.g., curves 2 and 4; Figures 10, 11b, and 13) are noticeably different from the measured amplitudes. These differences are more apparent when a comparison is made between the associated modeled seismograms (not shown here) and the observed seismograms. These comparisons corroborate our conclusion that only bright-spot velocities with misfit ≤ 0.5 should be considered as representing possible velocities of the bright spots.

To test whether interference of reflections from the different bright spots can produce its own AVO effect, biasing our observations, we repeated the modeling with a single diffraction point per bright spot and varied the spacing between the bright spots. We tested the case at which the reflection coefficient of a diffraction point is constant with respect to the angle of incidence. No consistent AVO pattern is observed in this case, only truncation of the overall reflection pattern when the spacing is larger than about 10 km. Such gaps also occur in our data and are accounted for by omitting traces with low combined P_xP and P_xS amplitudes. In the cases in which the diffraction points' reflection coefficient is a function of angle of incidence, the amplitude change with incidence-angle response

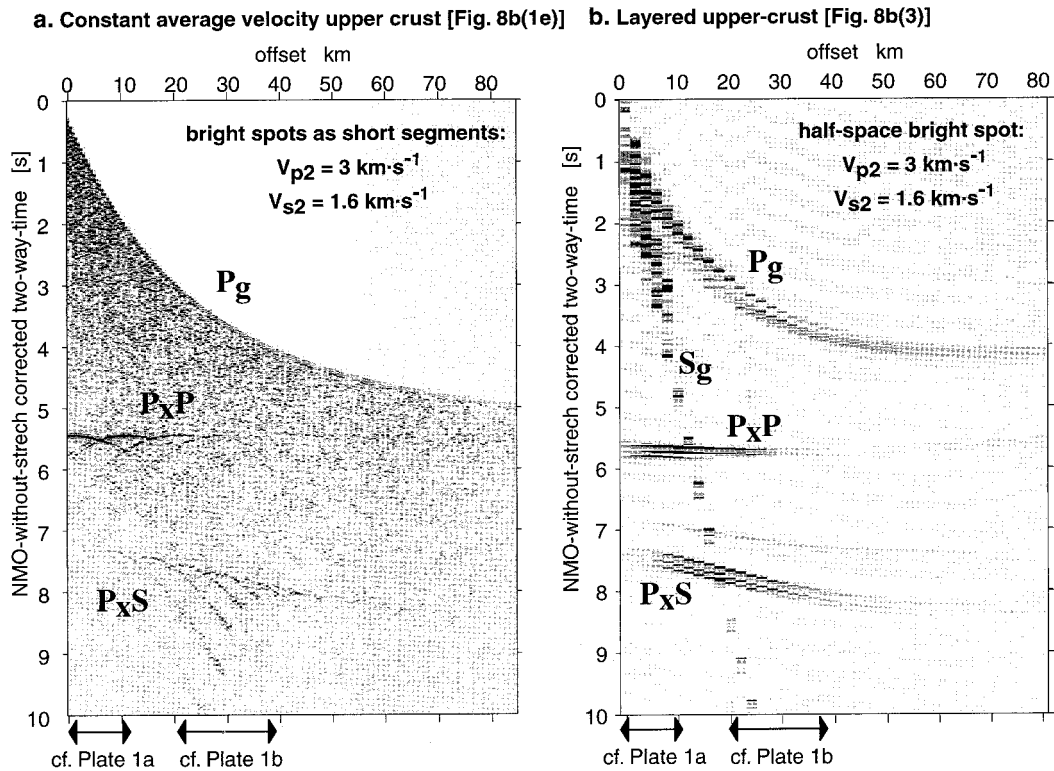


Figure 12. Synthetic vertical-component seismograms of the Tibetan bright-spot reflections modeled by the following: (a) The explicit reflectivity model (Figure 8b, explicit model) portraying the bright spots as 5-km-spaced diffracting segments in a constant average-velocity crust (see text). (b) The “layered” elastic reflectivity model (Figure 8b, model 3) portraying a layered upper crust above a half-space bright spot (see text). In both cases (Figures 12a and 12b) the bright spots are modeled with the same best velocities $V_{p2} = 3 \text{ km s}^{-1}$, $V_{s2} = 1.6 \text{ km s}^{-1}$ (Figure 11, circle 1), and a single-pulse zero-phase source waveform with 10 Hz center frequency. The synthetic amplitude-decay plots (Figure 3), waveforms (Figure 4b), amplitude gather (Figure 6b), and measured amplitudes (Figure 7b), are obtained from the synthetic seismograms in Figure 12a and the associated horizontal-component seismograms (not displayed). Offset ranges comparable to the coverage of the data examples in Plate 1 are marked. The AVO response of the data (Plate 1 and Figure 6a) are well modeled by the synthetics in both Figures 12a and 12b.

of a single diffraction point is matched closely by the overall AVO pattern when interpreted as coming from a single reflector.

We conclude that our approach to AVO analysis is self-consistent with our basic assumptions, and provides an adequate approximation for our observations.

6.2. Elastic Reflectivity Modeling

The Zoeppritz equations only allow direct calculation of reflection amplitudes from a single interface between two constant-velocity media. To examine the cases of a thin-layer bright-spot, and of variation with depth of upper crustal velocities, as well as our technique for measuring the amplitudes, we had to use a more robust procedure. We chose the 2-D Wideband Transfer Functions (OASP) and the pulse postprocessor (PP) modules of the OASES package [Schmidt, 1996; Schmidt and Glattetre, 1985] to calculate the exact solution to the elastic wave equation in horizontally stratified media by using the Direct Global Matrix technique [Schmidt and Tango, 1986] to determine the depth-dependent Green’s functions of the depth-separated wave equation. We calculated 20-s synthetic seismograms sampled at 100 Hz in the intercept time—slowness domain, resulting from a plane-wave originating at a compressional source pulse of a 5- to 15-Hz bandwidth. In all our models we represent the bright-spots by a velocity pertur-

bation with its top at 14.57 km depth. The effects of spherical spreading, attenuation, and noise were not included in our calculations. To measure the modeled AVO, we separately calculated the RMS of the vertical and horizontal components for each of the synthetic P_xP and P_xS phases. We then measured the RMS of the absolute amplitudes in a 1-s window centered on the reflected phase, the same procedure we used for measuring the data amplitudes. Our smoothed data-amplitude versus incidence-angle “ $B(i)$ curves” and their associated error bounds (Figure 9) were converted to amplitude versus slowness “ $B(p)$ curves” using, in keeping with our constant-velocity upper crust assumption, the relation $p = \sin(i)/V_{p1}$. The RMS misfit between our data and the model amplitudes, normalized by the error bounds (Figure 9), were then calculated for the slowness range 0.035 to 0.17 s km^{-1} (approximately equivalent to incidence angles of 10° to 65°). Several sets of parameters were modeled using spherical waves to produce offset-time domain synthetic seismograms (Figure 12b) which can be compared directly with the data and provide a test of the modeling results.

We used this elastic reflectivity methodology to examine three models shown in Figure 8b: (1) constant-velocity upper crust, (2) thin-layer bright spot, and (3) layered upper crust.

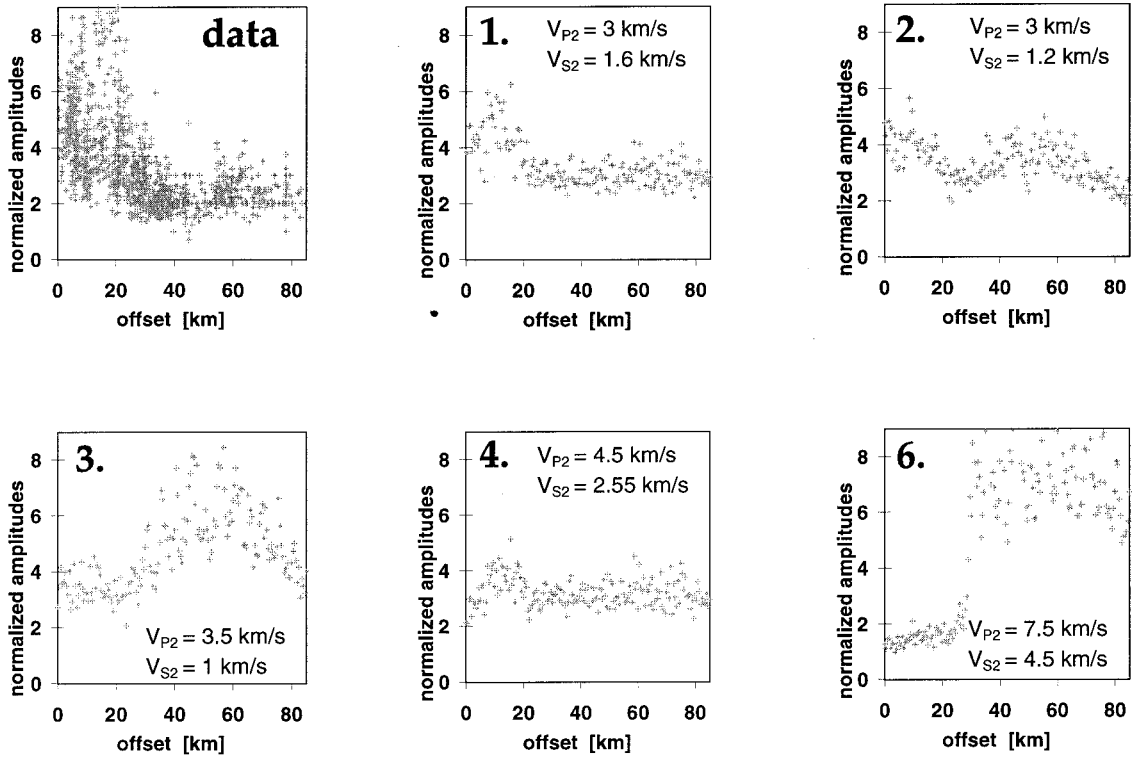


Figure 13. Normalized observed P_xP amplitudes (“data”; same as in Figure 7a) compared with synthetic normalized P_xP amplitudes modeled with the explicit reflectivity model (as in Figure 7b) for different bright-spot velocities (noted in each panel) and the same average crustal velocities. The scaling constant of (6) is applied to each panel to give equal average amplitudes. Numbers correspond to curves in Figure 10 and circles in Figure 11. This comparison confirms that modeled AVO curves with parameters outside the ≤ 0.5 misfit range of Figure 11b (panels 2 to 6) are significantly different from the observed AVO curve.

6.2.1. Simple elasticity model: Constant velocity upper crustal layer (with V_{p1} , V_{s1} , ρ_1 , and ρ_2 , as in the Zoeppritz model) above a half-space bright-spot (with varying V_{p2} and V_{s2}). This model (Figure 8b(1)) is equivalent to the Zoeppritz model, and the results, comparing curves 1 and ZE in Figure 14, and comparing Figure 15a with Figure 11b, show that the methods produce essentially the same results for $V_{p2} > 1.5 \text{ km s}^{-1}$. Note that models with $V_{p2} < 1.5 \text{ km s}^{-1}$ are presumably nonphysical as no common crustal material, not even pure water, has such low velocities under midcrustal pressure-temperature conditions. Testing this model with an alternative source bandwidth 0.5- to 2-Hz (Figure 14, curve 1a) results in flattening of the measured P_xP AVO curves at incidence angles lower than 20° , as in the curves measured from the data. This flattening is thereby shown to be an artifact of our measurement method that occurs because our 1-s measurement window is not large enough to include the full length of the P_xP phase at small incidence angles.

6.2.2. Thin-layer model: Constant-velocity upper crustal layer (as described above) and lower crustal half-space (same parameters) above and below a thin-layer bright spot. As discussed above, the bright spots appear on our data as a single-cycle phase which is either the reflection from a first-order interface (as modeled above) or the interference of reflections from the top and bottom of a layer with subresolution thickness. Constructive tuning occurs at near-vertical incidence when the layer thickness Δ is about quarter the wavelength λ of the P wave within the layer. In our model (Figures 8b(2) and 15b) the layer thickness is expressed by

$$\Delta = \frac{\lambda}{4} = \frac{V_{p2}}{4f} \quad (10)$$

where $f = 10 \text{ Hz}$ is the center frequency of our signal. The results (Figure 15b) show that only a low-velocity layer is in agreement with our measured AVO curves, and constrain essentially the same possible range of velocities V_{p2} and V_{s2} within this layer, as in the half-space model (Figure 15a). Inspection of the resulting modeled curves (Figure 14; curve 2) shows that they do not match the observed disappearance of P_xP amplitudes at incidence angles between 50° and 60° because of the persistence of the bottom reflection in the model. Variations of our thin-layer model with high attenuation within the layer, or 15% lower velocities below the layer, yield essentially the same result as the basic model.

Repeating this elastic reflectivity modeling with multiple alternating thin layers of fluid and solid produces a transversely anisotropic layer, but the results are still essentially the same. This result is in agreement with a maximum 5° shift in the angle of incidence of minimum P_xP amplitude on the AVO curves for a 20% anisotropy change that we calculated using a formulation for transverse anisotropy contrasts [Blangy, 1994] and also with the results for S wave AVO of Yardley *et al.* [1991].

The thin-layer model constrains essentially the same range of bright-spot parameters as in our simple half-space model, and although it provides a somewhat less good fit to our observed AVO than the half-space model, it is not clearly rejected by our data.

6.2.3. Layered model: Layered upper crust above half-space bright spot (with varying V_{p2} and V_{s2}). Although we do not have a highly detailed velocity model for the Tibetan upper crust, it is clear that it is not a single constant-velocity layer as in the above modeling. To test the importance of our constant-velocity assumption, we used a simplified horizontally layered velocity model (Figure 8b, model 3) that includes the major features of the upper crust as constrained by existing data. The top 1 km of the model is a one- or two-layer basin with average P wave velocity of 3 km s^{-1} , in agreement with the results of *Cogan et al.* [1998] for the northern Yadong-Gulu rift basins. Below, down to 5 km depth, is a layer of 5.7 km s^{-1} in agreement with the slope of P_g on our wide-angle supergather (Figure 6). A low-velocity layer, with $V_p = 5.3 \text{ km s}^{-1}$ and a gradational (nonreflective) upper boundary, stretches from a depth of 5 km down to the bright-spot reflector at 14.57 km. The necessity for such a layer has been shown by *Makovsky and Klempere* [1995] from the existence of an about 1-s step between semiparallel branches of P_g at an offset of about 100 km; is in agreement with velocity models constrained by INDEPTH teleseismic data [*Kind et al.*, 1996]; and is in agreement with the 5.3 km s^{-1} average velocity down to the bright spots shown in this paper (Figure 6a). The presence of this low-velocity layer can be explained by simple lithological changes, not necessarily related to the bright spots, or by the presence of minor pore-fluid content. V_{p1}/V_{s1} was held fixed at our measured average value of 1.65 throughout the upper crust of this model. As in the real data, the ray paths in this model are not straight lines, the angles of incidence are not explicitly known to us, and transmission losses occur in the upper crust. Yet our analysis of the synthetic seismograms was done assuming the same con-

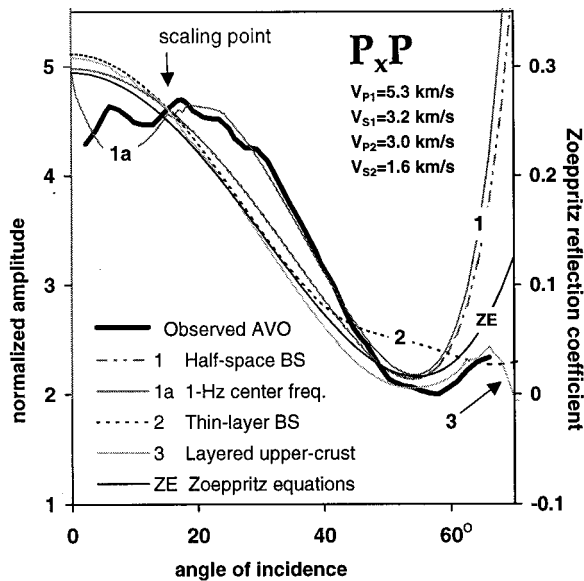


Figure 14. The match of the binned, smoothed P_xP AVO curve (Figure 9) with curves generated in our different models (Figure 8b) with the same preferred bright spot parameters. Curves 1, 2, and 3 were modeled by elastic reflectivity and correspond to the numbered circles of Figure 15. Curve 1a is as curve 1 but with a source of 1-Hz center frequency. Curve ZE was modeled with the Zoeppritz equations and corresponds to circle 1 in Figure 11. Although all curves are similar (see text) the half-space bright-spot models provide a somewhat better fit than the thin-layer model.

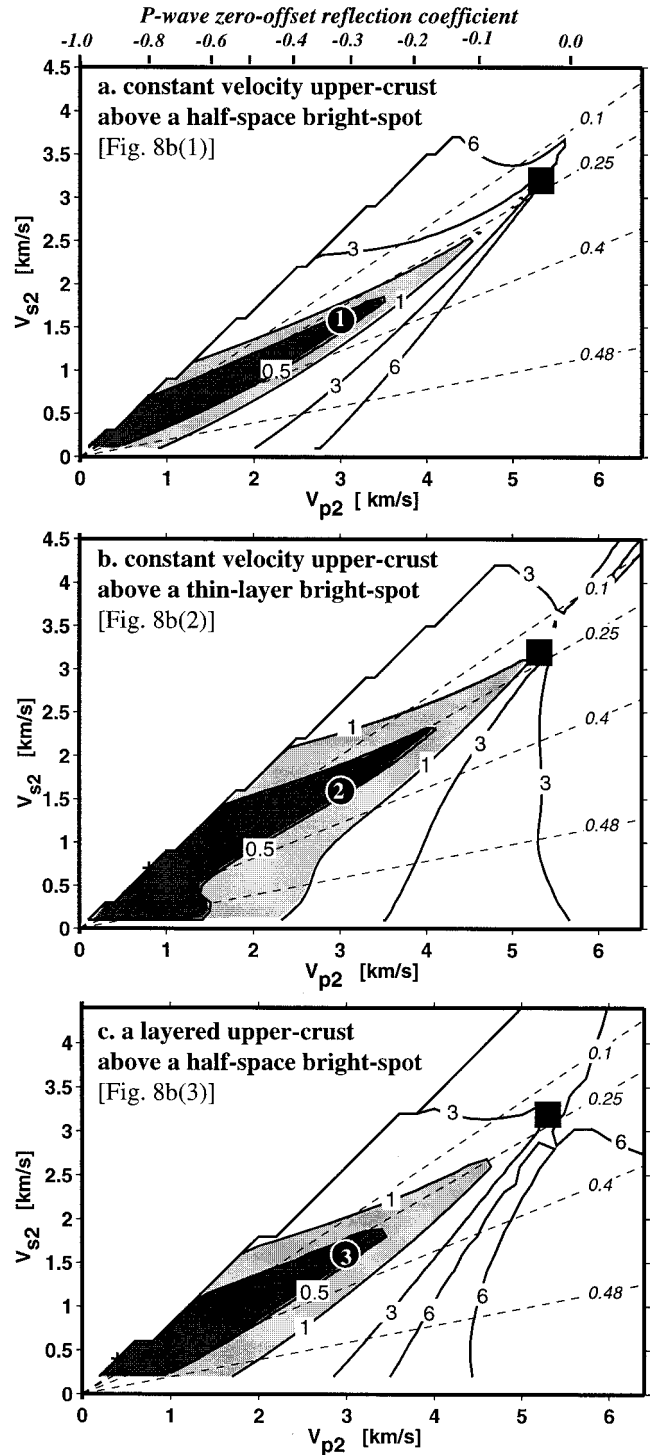


Figure 15. Normalized RMS misfit contours (results of elastic modeling) displayed as in Figure 11b for models of the three elastic classes discussed in the text. (a) Simple model—constant-velocity upper crust above a half-space bright spot (Figure 8b, model 1), the same model as in Figures 10 and 11. (b) Thin-layer model—thin-layer bright spot in a constant-velocity crust (Figure 8b, model 2). (c) Layered model—layered upper crust above a half-space bright spot (Figure 8b, model 3). Numbered circles correspond to modeled curves displayed in Figure 14. Similar results from all three models suggest the results are not model dependent.

stant-velocity upper crust as in all the above models. The misfit values, contoured in Figure 15c, are essentially the same as all previous models. Inspection of the actual modeled curves (Figure 14, curve 3) reveals that they are similar to models calculated with constant-velocity upper crust (Figure 14, curve 1) except that they reproduce the vanishing of amplitudes at incidence angles higher than 65° . This vanishing is due to evanescence of the down-going P-wave in shallow basins, turning to P_g instead of P_xP . The synthetic seismograms (Figure 12b) produced by this simple model (Figure 8b(3); Figure 15c, numbered circle) resemble the AVO response of the data and produce longer-duration waveforms than the explicit model (Figure 12a and 6b) in better agreement with the data (Plate 1 and Figure 6a). We conclude that although velocity structure and/or gradients in the upper crust provide a better fit to the data than the half-space model, their effects on the AVO response are negligible.

6.3. Modeling Conclusions and Error Estimates

In summary, our different elastic models all constrain essentially the same range of parameters as obtained by the simple Zoeppritz model, which shows that our results are not model dependent to any significant extent. That the AVO response in Figure 12 provided by the combination of reflections from different bright spots (Figure 12a) and the extended signal duration due to reverberations in the shallow basins (Figure 12b) reproduces the bulk of the complexity in the observed P_xP and P_xS waveforms (Plate 1) further demonstrates that the results of our AVO analysis are not model dependent. This, and the good resemblance of our synthetics (Figure 12) to the data (Plate 1), suggest that our results are also robust with respect to the 1-D assumption that underlies our supergather measurement procedure. We therefore conclude that the region with ≤ 0.5 normalized misfit (Figure 11b) bounds the likely range of the bright spots' seismic velocities. Note that this is a range of possible parameters that can produce a single observation, rather than being a range of different observations made by us. The acceptable range of velocities is in agreement with the vertical-incidence P wave reflection coefficient of the order of -0.4 ± 0.15 estimated by A. R. Ross et al. (submitted manuscript, 1998). Within the acceptable range, we conservatively prefer the values with higher P wave velocities, as these require the least amount of fluid to explain our observations. These P wave velocities are in agreement with the higher error bound on the vertical-incidence P wave reflection coefficient of A. R. Ross et al. (submitted manuscript, 1998), about -0.3 (Figure 11).

The significant possible error sources for our estimate above can be divided into three groups:

1. Errors in the normalization procedure due to the following: failure of the 1-D constant upper crustal velocity assumptions (due to velocity structure and gradients, or anisotropy in the upper crust); failure of the approximations implicit in (6); insufficient correction for source and receiver effects.
2. Distortion of the bright spots' AVO response due to internal structure, dip, or anisotropy of the bright spots.
3. Errors in the determination of the interval velocity immediately above the bright spots.

Since the primary feature in the data that controls our results is the incidence angle at which the P_xP amplitude reaches its minimum, we can evaluate the importance of each possible source of error by the deviation it could possibly introduce in the determination of that angle. From examination of the

contour plot of incidence angle of minimum P_xP (Figure 11a) we see that the angle of 55° we evaluate from our data based to our assumptions is as high as possible (for physical velocities, $V_p > 1.5 \text{ km s}^{-1}$). Thus errors that would imply higher angles are not physically interesting. Comparing the plots in Figure 11 shows that our contour of 0.5 misfit (Figure 11) represents angles of minimum P_xP amplitude of $\geq 45^\circ$ and is thus equivalent to $\pm 10^\circ$ error bar. This error bar represents the scattering of our normalized measured amplitudes around the smoothed median curve. Thus this error bar represents all local effects that were not removed by our normalization procedure: local dips and focusing of the bright spots; residual source and receiver variations; fine velocity structure in the upper crust (including the shallow basins); effects of scattered crustal reflectivity; and others. The consistency of the results of our various models demonstrates that the same error bars are robust with respect to: scattered crustal reflectivity (explicit model, Figure 8b(1e)); the internal structure and anisotropy of the bright spots ("thin layer" model, Figure 8b(2)); and upper crustal velocity structure and gradients (layered model, Figure 8b(3)). Anisotropy in the upper crust may cause the bending of the reflected wave ray paths, thus bias our estimate of incidence angle. However upper crustal anisotropy is unlikely to be greater than 10% [Crampin, 1994], thus is of the scale of velocity variations already considered by us in our layered model. The lack of measurable shear-wave splitting of the P_xS phase also implies negligible anisotropy. A consistent dip of the bright spots might shift our estimates of incidence angles. However, the amplitude curve measured using only shots southwest of receivers shows no systematic difference from the curve using only shots to the northeast of receivers, thereby ruling out the importance of a consistent dip in biasing our measured curves.

The only important possible source of systematic error in our analysis is due to errors in the estimate of interval velocities immediately above the bright-spot reflecting interface. Errors in average (kilometer-scale) interval velocities above the bright spots would similarly bias both our estimate of the bright-spots host rock properties (see discussion below) and the range of possible bright-spot velocities (Figure 11b). Thus such errors would have little effect on the results of the analysis below. Small-scale velocity perturbations with respect to a smooth velocity function are a major possible source of error, as these would bias only the range of bright-spot velocities resulting from our AVO analysis. Holliger [1996] measured a standard deviation of $\pm 0.3 \text{ km s}^{-1}$ sonic-log P wave velocity perturbations in deep boreholes with respect to a smooth upper crustal velocity model, and Jones and Holliger [1997] show that the S wave velocity perturbation distribution is proportional to the P wave perturbation (about 5% of the average velocity). We explicitly modeled the effect of these velocity error ranges, and we consider the ≤ 0.5 misfit range of Figure 12c to represent an upper bound on the ≤ 0.5 range of Figure 12b. We believe this overestimates our error because of the following:

1. The frequency of the sonic log (about 100 Hz) is much higher than the frequency of our measured waves (10 to 20 Hz), causing Holliger [1996] to measure larger velocity perturbations than applicable in this study.
2. P and S velocities directly above the bright spots are almost certainly correlated, either both higher or both lower than our measured average velocities, whereas our error mod-

eling also considered the anticorrelated cases [Jones and Holliger, 1997].

3. The fact that no clear reflectivity has been imaged in the Tibetan upper crust over about 2 s (about 5 km) above the bright spots (Figure 2 and Plate 1) suggests smaller velocity perturbations than measured by Holliger [1996] and Jones and Holliger [1997] in areas of seismically reflective upper crust [e.g., Emmermann and Lauterjung, 1997, Plate 3].

We believe that the ≤ 0.5 misfit ranges of Figures 11b and 11c are ample estimates of the error bounds of our analysis.

7. Geologic Interpretation of the Modeled Elastic Parameters

Project INDEPTH results suggest that the bright spots imaged in the Tibetan middle crust represent concentrations of fluids, whether aqueous fluids or melt [Nelson et al., 1996]. In this paper we have constrained the range of P and S wave velocities (Figure 16a) that can produce the Tibetan bright spot's observed AVO response. A. R. Ross et al. (submitted manuscript, 1998) used INDEPTH CMP data to constrain the zero-offset reflection coefficient of these same bright spots to about -0.4 ± 0.15 . These two independently obtained results are in good agreement and supplement each other, as demonstrated by overlaying our and A. R. Ross et al. (submitted manuscript, 1998) results (Figure 16a). The range of acceptable bright-spot P wave velocities implied by A. R. Ross et al. (submitted manuscript, 1998), $\leq 3.5 \text{ km s}^{-1}$ (Figure 16a), was calculated from our simple model (Figure 8b, model 1) taking into account our error bars for the interval velocity above the bright spots (as in Figure 11c). Note that the significant density contrast embedded in our simple model (-100 kg m^{-3}) results in low estimates for the P wave velocity contrast implied by the range of zero-offset reflection coefficients (Figure 16a). The bright-spot velocities constrained by these combined wide-angle and near-vertical results allow us to investigate the nature of the fluids concentrated at the bright spots. The alignment of the Tibetan bright spots at a similar depth along about 150 km of INDEPTH profile suggests that the fluids they represent are in at least quasi-static equilibrium at that depth, rather than representing a transient phenomenon. In the middle crust these fluids are therefore presumably at essentially lithostatic pressure, and form saturated pores (inclusions) in the rock [Mavko, 1980; Stocker and Gordon, 1975; Thompson and Connolly, 1990; Wood and Walther, 1986]. An intuitive way to examine porous rocks is the V_p - V_s plot (Figure 16b), in which the seismic velocities of a fluid-saturated porous rock lie on some mixing curve (weighted-average) between the velocities of the dry nonporous solid mineral assemblage ("rock point") and the velocities of the fluid filling the pores ("fluid point") [Castagna et al., 1985]. A reasonable approximation for the frame-forming rock of the bright spots is given by the elastic parameters V_{p1} , V_{s1} , and ρ_1 of the upper crust above the bright spots as defined above or of a granitic rock (Table 2). The fluid point for aqueous fluids, which at 15 km depth are probably supercritical H_2O and CO_2 [Krauskopf and Bird, 1995], are here represented by the parameters of H_2O at 0.4 to 0.5 GPa and 400° to 600°C (Table 2). The fluid point for partially molten silicates is constrained by the elastic parameters of pure natural silicate melts (their high-temperature liquidus parameters), and has only weak dependence on the melt composition (of natural melts) or the confining pressure [Murase and McBirney, 1973; Rivers and Carmichael, 1987; Wa-

tanabe, 1993]. Following the example of Watanabe [1993] we use the elastic parameters of andesitic melt (Table 2) [Murase and McBirney, 1973] for the fluid point of melt. This assumes that the temperature dependence of the elastic parameters of partial melt is due to the change in melt fraction. Andesitic melt probably provides a low-velocity (low-viscosity) bound for melts that may be present in the middle crust of southern Tibet: more-silicic melts are much higher viscosity, hence higher velocity, except at extreme temperatures close to their liquidus.

A mixing curve, characterizing a fluid-saturated porous rock, on the V_p - V_s plot (Figure 16b), depends on the end points, fluid and rock, and on the geometry of pores in the rock [Kuster and Toksöz, 1974]. A point along that curve is determined by the porosity, or fluid volume-fraction [Krief et al., 1990]. For an isotropic rock we can, without making assumptions about pore geometry or porosity, bound the possible range of mixing curves on the V_p - V_s plot between any specified fluid and rock by using the Hashin-Shtrikman upper and lower bounds [Hashin and Shtrikman, 1963]. On this plot (Figure 16c) our results—the range of acceptable bright spot velocities—lie clearly within the bounds for aqueous fluid, but only the extreme bounds of our error estimate cross the melt upper bound. Therefore the velocities constrained by our AVO analysis, taken with the vertical-incidence reflection coefficient estimated by A. R. Ross et al. (submitted manuscript, 1998) strongly suggest that pores saturated with aqueous fluids produce the bright-spot reflections we observe in the Tibetan middle crust. The alternative that the bright-spot reflections are produced by the presence of partial fraction of melt is unlikely but cannot be precluded based on the Hashin-Shtrikman bounds. However, this alternative that the presence of melt produces our seismic observations requires the melt-saturated rock to have P wave velocities $\leq 3.5 \text{ km s}^{-1}$, essentially the velocity of fully molten rock at its liquidus. Silicic intermediate melts have P wave velocities $\leq 3.5 \text{ km s}^{-1}$ only close to their liquidus, at temperatures in excess of 2000 K [Vo-Thanh et al., 1996], and even mafic melts have P wave velocities $\leq 3.5 \text{ km s}^{-1}$ only at temperatures in excess of 1200 K [Murase and McBirney, 1973; Rivers and Carmichael, 1987]. Such high temperatures are most unlikely to exist at 15 km depth in the Tibetan crust (C. Ruppel and D. McNamara, submitted manuscript, 1998). Introduction of anisotropy due to preferentially oriented cracks will tend to move the curves in the direction of increasing V_p (Figure 16b), in less good agreement with our results, and will only move the melt bounds further from our modeled velocities.

To estimate the fluid volume fraction we have to assume a certain pore geometry [Kuster and Toksöz, 1974]. On the basis of wetting properties of H_2O and CO_2 [Watson and Brenan, 1987] and melt [Laporte, 1994; Laporte et al., 1997], Watanabe [1993] (after Mavko [1980] and Schmeling [1985]) modeled the pores as triangular tubes forming an interconnected net at the intersection of grain boundaries and compared the velocities resulting when melt or H_2O saturate pores in a granitic rock at a depth of 15 to 20 km. Watanabe's [1993] velocity curves fall near the Hashin-Shtrikman upper bound and provide an upper estimate of about 15 to 20% aqueous fluid fraction in the Tibetan bright spots and about 5% in the rock above them. A similar fraction of aqueous fluids in interconnected tubes [Hyndman and Shearer, 1989] is also suggested by the low resistivity, about 1 Ωm , measured for the Tibetan bright spots [Chen et al., 1996], providing a better explanation than melt

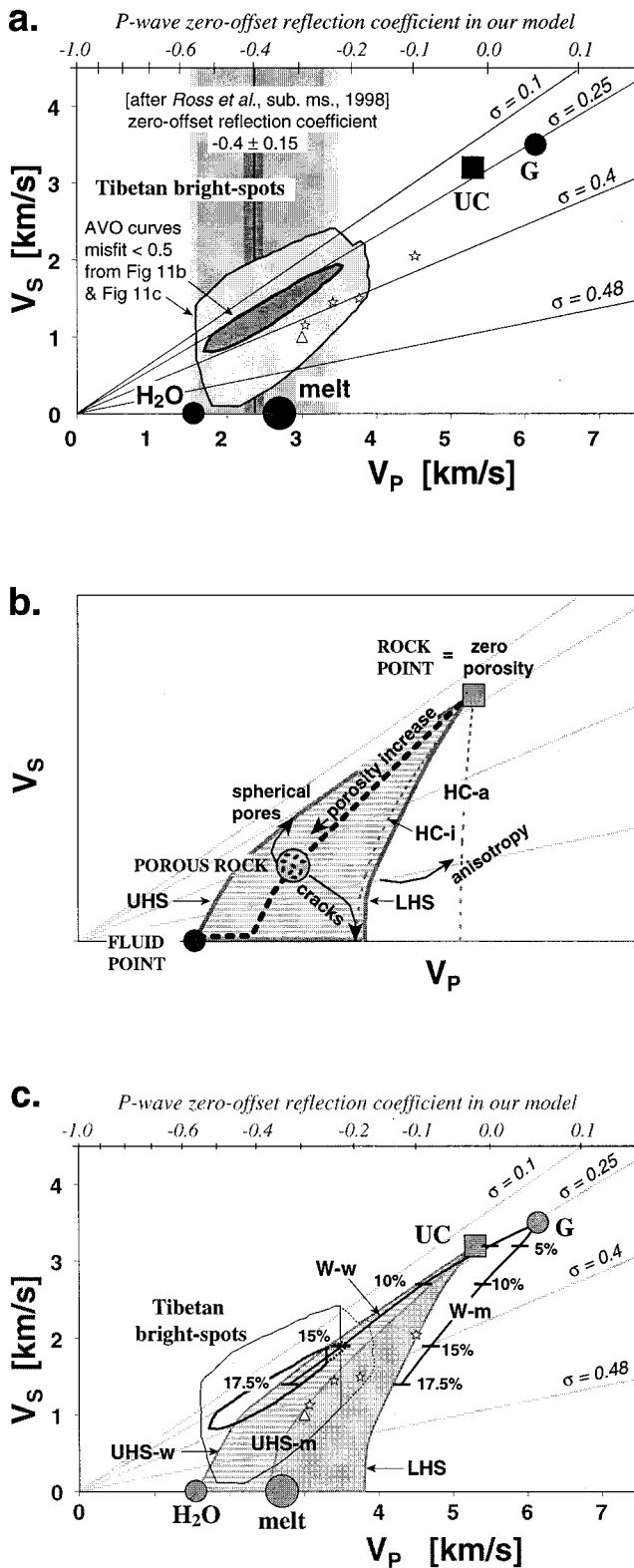


Figure 16. Nature of the fluids generating the Tibetan bright spots from our AVO analysis and theoretical bounds on the velocities of saturated rocks [e.g., *Mavko et al.*, 1998]. (a) Seismic velocities of the Tibetan bright spots and other basement bright spots. For the range of constrained bright-spot velocities, and their error estimates, we use the ≤ 0.5 normalized-misfit contours from Figures 11b and 11c (thick and thin black solid contours, with light and dark gray fill, respectively). Vertical black line marks the P wave velocity implied by Ross et al. (submitted manuscript, 1998) zero-offset reflection coefficient as calculated from our simple velocity model (Figure 8b, model 1), and vertical gray strips mark (in order of decreasing shade) the error ranges of this velocity due to our $\pm 0.3 \text{ km s}^{-1}$ error estimate for the interval velocity above the bright spots (V_{p1}); the error estimates ± 0.14 of Ross et al. (submitted manuscript, 1998); and the errors on this range due to our errors in V_{p1} . For comparison, we plot velocities measured by *Hussenoeder et al.* [1996] from the East Pacific Rise axial magma chamber (stars); and by *Lidaka et al.* [1993] for a shear-wave reflector (triangle) at about 20 km depth beneath the volcanically active Beppu-Shimabara graben, near Unzen volcano, Japan. Gray circles and square mark the velocities of rocks (granite (G)) and our measurement for the upper crust (UC) and fluids (H₂O and melt) mentioned in our discussion (Table 2). Oblique gray lines are lines of constant Poisson ratio (σ). (b) Velocities of a saturated porous rock (gray dotted circle) on a V_p - V_s plot. Seismic velocities of the bright spots, representing a fluid-saturated rock, lie on a mixing curve (thick dashed black line) between the velocities of country rock (rock point; light gray square) and the velocities of pure fluid (fluid point; dark gray circle). In the isotropic case, the range (filled with horizontal lines) of possible mixing curves is bounded by the Hashin-Shtrikman upper (UHS) and lower (LHS) bounds (thick gray lines) [*Hashin and Shtrikman*, 1963]. Within this range increasing porosity shifts velocities along a mixing curve toward the fluid point, but the appropriate mixing curve depends on the pore geometry. More spherical pores shift the curve toward UHS and for constant porosity shift velocities along that mixing curve towards the rock point, whereas more crack-like pores shift the curve toward LHS and, for constant porosity, shift velocities toward the fluid point. Anisotropic mixing curves may lie outside the isotropic range with higher V_p . Dry moduli for mixing curves of cracked media were calculated using Hudson's model [*Hudson*, 1981] then saturated moduli were calculated with the *Gassman* [1951] equation. These mixing curves (dashed gray lines) for the isotropic (Hudson cracks—*isotropic* (HC-i)) and the transversely anisotropic (HC-a) cases demonstrate the effects of cracks. (c) The combined results from our AVO analysis and Ross et al. (submitted manuscript, 1998) zero-offset reflection coefficient (as shown in a) superimposed on the Hashin-Shtrikman upper and lower bounds (thick gray lines) for melt (vertical lines) and H₂O (horizontal lines): LHS, lower Hashin-Shtrikman bound (the same for melt and H₂O); UHS-m, upper Hashin-Shtrikman bound for melt; UHS-w, upper Hashin-Shtrikman bound for H₂O. Rock and fluid points (Table 2) are marked as gray shapes and labeled as in Figure 16a. Velocities from other basement bright-spots (stars and triangle as in Figure 16a) are projected for comparison (note rock points for these measurements are probably somewhat different than our case). The V_p - V_s mixing curves (labeled black lines) calculated by *Watanabe* [1993] for H₂O (W-w) and melt (W-m) at grain intersections of a granitic rock, and their associated porosities (numbered horizontal bars), provide an upper bound H₂O-content estimate for the bright spots, and the upper crust above them, of about 15 to 20% and 5% respectively.

[Jones, 1992; Schilling *et al.*, 1997] for these resistivity observations. The introduction of randomly oriented cracks [Hudson, 1981; O'Connell and Budiansky, 1974] would reduce the estimated fluid fraction considerably but would also move the curves in the direction of increasing V_p (Figure 16b), putting them in less good agreement with our results.

We conclude that the Tibetan bright-spot reflections represent a series of aqueous fluid concentrations, each about 1 to 2 km wide laterally and containing about 10% fluid by volume. The aqueous fluids dominate the seismic response of the Tibetan bright spots, but we cannot rule out the additional presence of some partial-melt fraction at or beneath these bright spots. The measured AVO response of the Tibetan bright spots is in better agreement with single-reflector-over-half-space models than with thin-layer models, but it is clear that the bright spots must be limited in their depth extent. This seeming discrepancy is probably a result of a gradual increase of velocity below the reflector rather than a sharp contact at the bottom of the Tibetan bright spots. Such a gradual velocity increase can result if the fluid concentration is greatest in the tens of meters near the top of the bright spot and diminishes with depth or if the aqueous fluids are concentrated at the top of a partial melt layer or both. Hence our results are in agreement with the variable-velocity layering suggested for the Tibetan bright spots based on higher-frequency data (A. R. Ross *et al.*, submitted manuscript, 1998) and for the Socorro bright spot [Ake and Sanford, 1988; Brocher, 1981]. The alignment of the bright spots at a relatively constant depth along about 150 km of the INDEPTH profile suggests to us that they represent a pressure temperature, rather than structurally, controlled phenomena. We next briefly discuss two end-member models for the thermal state of the Tibetan bright spots, both of which require a crustal heating event, presumably as a result of the doubling in the thickness of the Tibetan plateau crust [England and Thompson, 1984; Henry *et al.*, 1997]:

1. The first end-member model postulates that the bright spots form as concentrations of free aqueous fluids on top of a cooling partial-melt body. Wet crustal melts collect from the partially melted middle crust [Nelson *et al.*, 1996; Hirn *et al.*, 1997] and rise until their temperature approaches their solidus at which point they stop and crystallize. In this process the melt phase saturates, and a free H₂O-rich phase separates and collects, possibly in pegmatitic intrusions, at the top of the magmatic body [Jahns, 1982] producing the bright-spot characteristics. Support for this model may derive from exposures of felsic pegmatites in the footwall of the Nyainqentanglha detachment, at the northwest boundary of the northern Yadong-Gulu rift, which have been exhumed from about 10 to 15 km depth since 8 Ma [Harrison *et al.*, 1995]. This end-member model constrains the maximum possible temperature and heat flow that can be present for any significant length of time, at about 15 km depth beneath the Yadong-Gulu rift. The maximum temperature of free H₂O-rich aqueous fluids is bounded by the wet solidus of granite, about 650°C at the pressure of 0.4 to 0.5 GPa [Luth *et al.*, 1964]. This temperature at 15 km depth implies a maximum conductive surface heat flow of about 110 mW m⁻² [Chapman and Furlong, 1992], substantially lower than the values measured by Francheteau *et al.* [1984] but in agreement with the estimates of Hochstein and Yang [1995] and Hochstein and Regenauer-Lieb [1998]. The inferred lower heat flow than measured by Francheteau *et al.* [1984] suggests that convective heat flow, possibly also in a deep-reaching hydro-

thermal system, is at least locally important in the Tibetan upper crust.

2. The other end-member model postulates a metamorphic source for the aqueous fluids concentrated at the bright spots. This model is compatible with temperatures significantly lower than the granite wet solidus, and therefore is easier to reconcile with the cool upper mantle suggested to exist beneath southern Tibet. This model depicts a heat front that is propagating through crustal material beneath southern Tibet and causing metamorphic dehydration [e.g., Connolly and Thompson, 1989]. Dehydration of pelitic rocks, which probably constitute a major component of the upper midcrust beneath the northern Yadong-Gulu rift [Harrison *et al.*, 1995], could provide a local source of H₂O-rich aqueous fluids [Thompson, 1982; Fyfe *et al.*, 1978] for the bright spots. Alternatively, the source of fluids may be dehydration of the Indian crust, underthrusting southern Tibet with its top at about 60 to 70 km depth [Owens and Zandt, 1997], or Tethyan passive margin imbricates, postulated to be present in the lower crust of southern Tibet (Y. Makovsky *et al.*, INDEPTH wide-angle profiling traces midcrustal reflector: An ophiolitic slab beneath the India-Asia suture in southern Tibet?, submitted to *Tectonics*, 1998) as they heat to about 550°–700°C [Henry *et al.*, 1997; Le Pichon *et al.*, 1997]. The concentration of these fluids at the bright spots would occur at a lithological aquitard [Connolly and Thompson, 1989; Thompson and Connolly, 1990; Bailey, 1994] or at a mechanical barrier like that suggested to exist at the brittle-ductile transition [Bailey, 1990; Hyndman and Shearer, 1989] at about 300° to 400°C. The bright spots might result from transient changes in the rate of fluid flow at this level, possibly similar to the about 10% porosity “water sills” proposed by Connolly [1997] and Connolly and Podladchikov [1998].

Either end-member model postulates an upward flow, possibly episodic [e.g., Connolly, 1997], of aqueous fluids (as free fluids or incorporated in melt) through the middle crust in southern Tibet, i.e., a “wet” middle crust. High concentration of Cl⁻ [Zhang, 1986; Hochstein and Yang, 1995] and traces of ³He [Hoke *et al.*, 1996] in water of the Yangbajain geothermal springs and wells provide evidence for a contribution of deep saline waters to these springs. If the source of fluids is from the underthrusting Indian crust or the Tethyan passive margin imbricates above it, the implication is that the fluids percolate through the southern Tibet middle crust, whether in melt or as free aqueous fluids. The presence of free aqueous fluids would then weaken the middle crust [Etheridge *et al.*, 1984] and allow for the development of midcrustal flow [Royden, 1996], similar to that suggested by Nelson *et al.* [1996] to occur due to the presence of melt. A more comprehensive analysis is needed to evaluate the thermal and mechanical implications of the presence of free aqueous fluids in the southern Tibet middle crust.

Our observations bear on the long-lived debate about the extent to which free aqueous fluids are present in interconnected pores in the middle to lower continental crust [e.g., Yardley and Valley, 1994]. The presence of such fluids in minor amounts (<1%), is commonly postulated on the basis of widespread high electrical conductivity and its common correlation with seismic reflectivity in stable continental lower crust [e.g., Hyndman and Shearer, 1989]. In contrast an essentially “dry” stable continental lower crust is commonly postulated based on the petrologic argument that all free fluids are consumed rapidly by retrograde reactions with high-grade anhydrous minerals [e.g., Yardley and Valley, 1997]. Recent results from the

KTB deep drill hole [Emmermann and Lauterjung, 1997, and references therein] demonstrate the presence of aqueous fluids deep into the brittle continental upper crust, yet also suggest that high electrical conductivity can result from the presence of graphite films in shear zones. Although seismic reflectivity has served as a major argument in this debate about the source of crustal conductivity the interpretation that seismic reflectivity marks the presence of aqueous fluids has always been based on circumstantial geological evidence. In this paper we provide a direct measurement of the physical properties producing the observed seismic reflections, then we use rock physics results to show that our observations most probably result from the presence of the order of 10% free aqueous fluids. Although our measurements were made in an active orogenic zone, our approach (and potentially the large volume fraction of fluids we observe) should be extrapolated to other areas of the continents.

8. Conclusions

We present the results of quantitative analysis of the bright spots, imaged in southern Tibet by project INDEPTH, based on our three-component single-fold wide-angle data. We measured the amplitudes of P_xP and P_xS reflections, developed and applied a methodology to normalize these amplitudes with respect to source, receiver, and amplitude losses along the travel path, and found a consistent variation of amplitude with incidence angle. The merging of reflections from multiple bright spots provided adequate angular coverage for AVO analysis, and reliably allowed us to estimate both P and S wave velocities of the bright-spots to be $3.0 \pm 0.8 \text{ km s}^{-1}$ and $1.6 \pm 0.8 \text{ km s}^{-1}$, respectively. Adding the constraint of near-vertical P wave reflection coefficient (A. R. Ross et al., submitted manuscript, 1998) further constrains the P wave velocity to be $\leq 3.5 \text{ km s}^{-1}$. These velocities, when considered in the light of theoretical and experimental rock physics, imply that regionally extensive, free aqueous-fluid concentrations in the Tibetan middle crust produce the observed seismic bright-spot reflections. Because of this remarkable implication, we conducted extensive modeling to demonstrate the robustness of our methodology to all likely sources of error. We conclude that our data are indeed best fit by about 10% free water at about 15 km depth.

Appendix A: Testing the Validity of Our Correction Scheme

The amplitude of the scattered crustal reflectivity has a characteristic decay-curve shape on seismogram amplitude plots (e.g., Figure 3), which is controlled by the path-dependent loss term L (equation (8)). Our normalizing procedure (equation (6)) assumes that the median of the source-generated signal $\langle A_s \rangle$ (our normalizing factor) is a measure for the general amplitude decay of the seismogram which is not affected by any specific seismic phase (particularly not by the bright-spot reflections), approximates $A_s(T)$, and thus (from equation (5)) scales only to the source, receiver, and path-dependent-loss terms of (4). To gain confidence in the results of our analysis it is important to test the reliability of our normalizing factor, particularly as a function of offset. The plot of our normalizing-factor values (one per trace) as a function of offset $\langle A_s(h) \rangle$ (Figure A1) shows a scatter of 3 orders of magnitude. To understand the significance of these values, we separate

$\langle A_s \rangle$ into its components in order of their relative effect on the trace amplitude. We expect the receiver term, R of (5), to have the largest relative effect because of 2 orders of magnitude variation in the sensitivity and dynamic range of our different sensor types (Table 1b). The variations in dynamic range between the receivers are apparent when the values of $\langle A_s(h) \rangle$ recorded at the different receivers are coded by different symbols (Figure A1a). The values for each receiver show a trend to lower values at higher offset, which corresponds with the theoretical trend of the path-dependent amplitude-loss term of (5), $L(T(h))$, calculated for a constant-velocity crust (using equation (8)) for the P_xP travel time T . To better examine the match of $\langle A_s(h) \rangle$ with $L(h)$, we separately estimated the receiver term by measuring the receiver-gained ambient noise level (N_0R of (5)) as the median amplitude of a 60- to 80-s reduced-time window. (Note that this estimate is not very good since it is based on noise; it is used here only for examining $\langle A_s(h) \rangle$ and is not used for our AVO analysis.) Dividing our normalizing factor $\langle A_s(h) \rangle$ by the receiver-gained ambient noise:

$$\frac{\langle A_s(s, r, h) \rangle}{N_0R(r)} \approx \frac{S(s)L[T(h)]}{N_0} + 1 \quad (\text{A1})$$

yields (Figure A1b) an estimate for the second-order amplitude effect in our data, the path-dependent loss term as a function of offset, $L[T(h)]$. Thus, in Figure A1b the trend of the values with offset corresponds mainly to the trend of the path-dependent term, $L[T(h)]$, with offset. The ratio $\langle A_s(h) \rangle / N_0R$ decreases by about 1 order of magnitude as offset increases from 0 to 80 km, in general agreement with the theoretical trend of the bright-spot reflection path-dependent-loss term $L[T(h)]$. The scatter of about 1 order of magnitude around this trend is mostly due to the source term S of (5). This can be demonstrated by dividing $\langle A_s(h) \rangle / N_0R$ by $L[T(h)]$ and plotting the result with respect to source location number (Figure A1c). The long-wavelength variation in Figure A1c (e.g., a minimum at about source number 500, maximum between sources 600 and 700, etc.) probably corresponds mostly to the structure of the shallow basins beneath the shot points, while variation of the source amplitude, and local variations (mostly in ambient noise) produce the remaining scatter. Figure A1a, A1b, and A1c show that our normalizing factor $\langle A_s \rangle$ does indeed scale to the amplitude-modifying terms for which we wanted to normalize the measured bright-spot amplitudes A_b (equation (4)) as assumed in (6).

We made additional tests for the reliability of our normalizing factor by analyzing, with the same methodology, realistic synthetic seismograms generated based on our basic assumptions by explicit reflectivity modeling (as discussed in the text). In this modeling, P wave crustal reflectivity dominates the amplitude of the seismogram (Figure 3) and decays solely as a function of the reflection two-way travel time due to spherical spreading and attenuation (equation (8)), as assumed in the derivation of (5) and (6). The attenuation is determined by the quality factor Q for which previously reported average upper crustal values are of the order of 50 to 1000 [Toksöz et al., 1990]. The values of $\langle A_s(h) \rangle / \langle A_s(100 \text{ km}) \rangle$ measured from seismograms modeled with quality factor $Q = 100$ and 200, and their trend with offset, are in agreement with our observed $\langle A_s(h) \rangle / N_0R$ values and their trend (Figure A1b). The modeled amplitude decay curves (Figure 3), amplitude gather (Figure 6b), and measured normalized amplitudes (Figure 7b), all correspond to their observed counterparts. Thus the basic as-

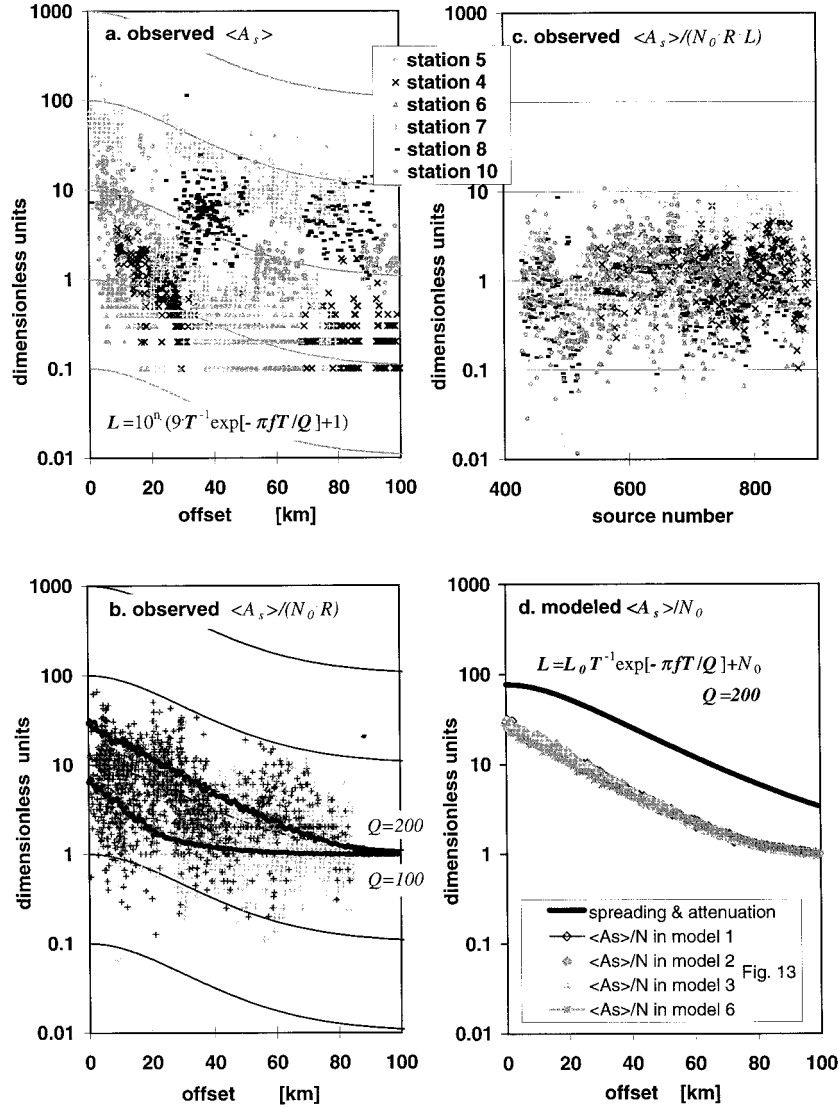


Figure A1. Dependence of our normalizing factor $\langle A_s \rangle$ (equation (6)) on offset, source, path, and receiver amplitude effects. (a) $\langle A_s \rangle$ values measured from our data (used to normalize our bright-spot reflections amplitude measurements), plotted logarithmically against offset. Different symbols denote the receivers (stations) by which the data was recorded. Horizontal streaks at values < 1 result from the resolution of our measured value (one decimal digit), a constraint of our processing software. Thin gray lines are theoretical decay curves, that is, the path-dependent loss term L in a constant-velocity and attenuation crust (equation (8)) calculated for the P_xP twt as a function of offset $L(T(h))$ and multiplied by a power of 10 (as noted in the figure). (b) Values shown in Figure A1a after normalization by $N_0 \cdot R$, the receiver-gained noise level (equation (A1)). Light gray crosses are measured from traces later omitted based on low combined P_xP and P_xS measured amplitudes. Thin black lines as in Figure A1a. Thick black lines (and dots) are synthetic values of $\langle A_s \rangle / N_0$ generated by the explicit reflectivity model (see Appendix A) with attenuation quality factors $Q = 100$ and 200 (N_0 is approximated by the modeled value of A_s at 100 km offset). (c) Values shown in (b) after normalization by $L(T(h))$, the path-dependent loss term (equation (8)) calculated for the variation of P_xP twt with offset (thin black line largely covered by data in Figure A1b). Values plotted by source number (corresponding approximately to source location). (d) Synthetic values of $\langle A_s \rangle / N_0$ measured from several runs of the explicit reflectivity model with the same average crustal velocities and attenuation, but different bright-spot velocities (N_0 is approximated by the modeled value of A_s at 100 km offset). Different symbols correspond to $\langle A_s \rangle$ values used to normalize the different models in Figure 13 (annotated on plot). Thick black line is the path-dependent term $L(T(h))$ actually used in the same model at P_xP twt T (as annotated on the plot; L_0 is the value at zero offset).

assumptions of our explicit reflectivity model, including the generation and role of $\langle A_s \rangle$, give an adequate representation of our data. We modeled several seismogram gathers with an identical set of crustal parameters (e.g., $Q = 200$) but differ-

ent bright-spot velocities, and generated significantly different normalized AVO curves (Figure 13, curves 1–6). A comparison of the curves of the normalizing factor with offset $\langle A_s(h) \rangle / N_0$ of these different models (Figure A1d) verifies

that these curves are essentially identical and are not biased by the AVO of the bright spots. A comparison of the change with offset of these modeled $\langle A_s(h) \rangle / N_0$ values (grey symbols in Figure A1d), to the change with offset of the path-dependent amplitude loss, applied in the same models at the two-way travel time of the bright spots $L(T(h))$ (black in Figure A1d), provides a test for the approximation of (6). The mismatch between the trends of these curves is negligible and would not bias our AVO measurement in a significant way. The above tests, taken together, give confirmation of our normalization approach and suggest the validity of the results of our analysis. We suggest that the applicability of our normalization approach to other data sets should be tested, as it might prove to be a powerful tool for the investigation of continental basement.

Notation

a_k	instantaneous amplitude of the k component of a trace.
$A(t)$	complex amplitude of a three-component seismogram as a function of time.
A_b	mean amplitude of a bright-spot reflected phase over a fixed time interval Δt .
$A_b(h)$	AVO of a bright-spot reflected phase, i.e., its amplitude as a function of source-receiver offset h .
A_s	mean amplitude of the background crustal reflectivity over a fixed time interval Δt .
$\langle A_s \rangle$	median of the complex amplitude $A(t)$ over the trace length 0–20 s; $\langle A_s \rangle$ is our normalizing factor.
$\langle A_s(h) \rangle$	approximation for the AVO of the crustal reflectivity.
$B(i, M)$	reflection coefficient of bright spots as a function of incidence angle and elastic moduli.
B_{cr}	the maximum reflection coefficient of the crustal reflectivity.
B_{XY}	bright-spot's reflection coefficient for incident X wave and reflected Y wave.
c	scaling constant.
Δ	layer thickness.
f	center frequency of a seismic wavelet.
ϕ_{xx}	projection of the xx arriving phase to the vertical component.
h	source-receiver offset.
i	incidence angle of a wave at a reflector.
i	the complex square root of -1 .
j, k	indices.
L	path-dependent loss due to spherical spreading, attenuation, etc.
λ	wavelength.
M	the set of elastic moduli above and below the interface.
N_0	ambient-noise amplitude level.
p	ray parameter (slowness).
Q	attenuation quality factor.
r	receiver number.
R	receiver response.
ρ	density.
s	source number.
S	mean amplitude of the source-generated signal.
t	recording time.
Δt	the duration of our measurement time window.

T	the bright-spot reflection two-way time.
$T_{XX}^{j,k}$	the two-way travel time of phase XX from the k th diffraction point of the j th bright spot.
T_{X_g}	the travel time of crustal direct-wave phase X_g .
θ_k	instantaneous phase of the k component trace.
v	the seismic-velocity structure traversed by the wave.
ψ_x	x component reflectivity series.

Functions

$\delta(t) = \begin{cases} 1 & t = 0 \\ 0 & t \neq 0 \end{cases}$	the delta function.
$H(t) = \begin{cases} 0 & t < 0 \\ 1 & t \geq 0 \end{cases}$	the step (Heavyside) function.

$\text{rand}(t)$ a random number in the range $[-1, 1]$ for every time t .

Seismic phases

P_xP	reflected P wave phase (P wave incident and P wave reflected).
P_xS	converted P to S wave reflection (P wave incident and S wave reflected).
S_xS	reflected S wave phase (S wave incident and S wave reflected).
S_xP	converted S to P wave reflection (S wave incident and P wave reflected).
P_g	direct crustal P wave.
S_g	direct crustal S wave.

Acknowledgments. We thank Boris Gurevich of the Geophysical Institute of Israel for assisting with the elastic modeling procedure; Ran Bachrach, Gary Mavko, Tapan Mukerji, and Li Teng for help with rock physics; George Thompson, Mark Zoback, Amos Nur, Tom Parsons, Bill Kidd, Juhn Liou, Carolyn Ruppel, an anonymous reviewer, and many others for helpful reviews and discussion. Tom Brocher's exceedingly detailed and thoughtful review engendered significant improvements. We thank the personnel of the 4th and 5th Geophysical Brigades of the Ministry of Geology and Mineral Resources, and the Stanford wide-angle field team, in particular Ian Billings, for their efforts. We thank the Project INDEPTH team, in particular Larry Brown, Doug Nelson, Doug Alsdorf, and Andy Ross for data transfer and advice. We thank the Stanford Rock Physics Project for the use of their resources. This work was supported by the Ministry of Geology and Mineral Resources of China, U.S. National Science Foundation Continental Dynamics Program (EAR-9316314), National Natural Science Foundation of China, Deutsche Forschungsgemeinschaft, IRIS-PASSCAL, and by GeoForschungsZentrum Potsdam (GFZ), Germany. Part of this work was done at Institute "Jaume Almera"-CSIC with support from the Spanish National Science Agency (UE95-0026).

References

- Ake, J. P., and A. R. Sanford, New evidence for the existence and internal structure of a thin layer of magma at mid-crustal depths near Socorro, New Mexico, *Bull. Seismol. Soc. Am.*, 78(3), 1335–1359, 1988.
- Aki, K., and P. G. Richards, *Quantitative Seismology: Theory and Methods*, 932 pp., W. H. Freeman, San Francisco, Calif., 1980.
- Allen, J. L., and C. P. Peddy, *Amplitude Variation With Offset: Gulf Coast Case Studies*, 126 pp., Soc. of Explor. Geophys., Tulsa, Okla., 1993.
- Alsdorf, D., L. D. Brown, K. D. Nelson, Y. Makovsky, S. L. Klemperer, and W. Zhao, Crustal deformation of the Lhasa terrane, Tibet Plateau from INDEPTH deep seismic reflection profiles, *Tectonics*, 17, 501–519, 1998a.
- Alsdorf, D., et al., INDEPTH (International Deep Profiling of Tibet and the Himalaya) multi-channel seismic reflection data: Description and availability, *J. Geophys. Res.*, 103, 26,993–26,999, 1998b.

- Armijo, R., P. Tapponnier, J. L. Mercier, and T. L. Han, Quaternary extension in southern Tibet; field observations and tectonic implications, *J. Geophys. Res.*, *91*, 13,803–13,872, 1986.
- Bailey, R. C., Trapping of aqueous fluids in the deep crust, *Geophys. Res. Lett.*, *17*(8), 1129–1132, 1990.
- Bailey, R. C., Fluid trapping in mid-crustal reservoirs by H₂O-CO₂ mixtures, *Nature*, *371*, 238–240, 1994.
- Barnes, A. E., and T. J. Reston, A study of two mid-crustal bright spots from Southeast Georgia (USA), *Geophys. J. Int.*, *108*(2), 683–691, 1992.
- Blangy, J. P., AVO in transversely isotropic media—an overview, *Geophysics*, *59*(5), 775–781, 1994.
- Bowers, T. S., Pressure-volume-temperature properties of H₂O-CO₂ fluids, in *Rock Physics and Phase Relations: A Handbook of Physical Constants, Ref. Shelf Ser.*, vol. 3, edited by T. J. Ahrens, pp. 45–72, AGU, Washington, D. C., 1995.
- Brocher, T. M., Geometry and physical properties of the Socorro, New Mexico, magma bodies, *J. Geophys. Res.*, *86*, 9420–9432, 1981.
- Brown, L., et al., COCORP: New perspectives on the deep crust, *Geophys. J. R. Astron. Soc.*, *89*(1), 47–54, 1987.
- Brown, L. D., W. Zhao, K. D. Nelson, M. Hauck, D. Alsdorf, A. Ross, M. Cogan, M. Clark, X. Liu, and J. Che, Bright spots, structure, and magmatism in southern Tibet from INDEPTH seismic reflection profiling, *Science*, *274*(5293), 1688–1690, 1996.
- Calvert, A. J., and R. M. Clowes, Deep, high-amplitude reflections from a major shear zone above the subducting Juan de Fuca Plate, *Geology*, *18*(11), 1091–1094, 1990.
- Cameli, G. M., I. Dini, and D. Liotta, Upper crustal structure of the Larderello geothermal field as a feature of post-collisional extensional tectonics (southern Tuscany, Italy), *Tectonophysics*, *224*(4), 413–423, 1993.
- Castagna, J. P., and M. M. Backus, Offset-dependent reflectivity: Theory and practice of AVO analysis, in *Investigations in Geophysics Series*, edited by M. R. Cooper, pp. 348, Soc. of Explor. Geophys., Tulsa, Okla., 1993.
- Castagna, J. P., M. L. Batzle, and R. L. Eastwood, Relationships between compressional-wave and shear-wave velocities in clastic silicate rocks, *Geophysics*, *50*(4), 571–581, 1985.
- Chapman, D. S., and K. P. Furlong, Thermal state of the continental crust, in *Continental Lower Crust*, edited by D. M. Fountain, R. Arculus, and R. W. Kay, pp. 179–200, Elsevier, New York, 1992.
- Chen, L., J. R. Booker, A. G. Jones, N. Wu, M. J. Unsworth, W. Wei, and H. Tan, Electrically conductive crust in southern Tibet from INDEPTH magnetotelluric surveying, *Science*, *274*(5293), 1694–1696, 1996.
- Chun, K., and T. Yoshii, Crustal structure of the Tibetan Plateau: A surface-wave study by a moving-window analysis, *Seismol. Soc. Am. Bull.*, *67*(3), 735–750, 1977.
- Cogan, M., K. D. Nelson, W. Kidd, C. Wu, and Project INDEPTH Team, Shallow structure of the Yadong-Gulu rift, southern Tibet, from refraction analysis of INDEPTH CMP data, *Tectonics*, *17*(1), 46–61, 1998.
- Connolly, J. A. D., Devolatilization-generated fluid pressure and deformation-propagated fluid flow during prograde regional metamorphism, *J. Geophys. Res.*, *102*, 18,149–18,173, 1997.
- Connolly, J. A. D., and Y. Y. Podladchikov, Compaction-driven fluid flow in viscoelastic rock, *Geodin. Acta*, *11*(2–3), 55–84, 1998.
- Connolly, J. A. D., and A. B. Thompson, Fluid enthalpy production during regional metamorphism, *Contrib. Mineral. Petrol.*, *102*, 347–366, 1989.
- Crampin, S., The fracture criticality of crustal rocks, *Geophys. J. Int.*, *118*, 428–438, 1994.
- Emmermann, R., and J. Lauterjung, The German Continental Deep Drilling Program KTB: Overview and major results, *J. Geophys. Res.*, *102*, 18,179–18,201, 1997.
- England, P. C., and A. B. Thompson, Pressure-temperature-time paths of regional metamorphism, I, Heat transfer during the evolution of regions of thickened continental crust, *J. Petrol.*, *25*(4), 894–928, 1984.
- Etheridge, M. A., V. J. Wall, and S. F. Cox, High fluid pressures during regional metamorphism and deformation: Implications for mass transport and deformation mechanisms, *J. Geophys. Res.*, *89*, 4344–4358, 1984.
- Fielitz, K., Elastic wave velocities in different rocks at high pressure and temperature up to 750°C, *Z. Geophys.*, *37*, 943–956, 1971.
- Francheteau, J., C. Jaupart, X. J. Shen, W. H. Kang, D. L. Lee, J. C. Bai, H. P. Wei, and H. Y. Deng, High heat flow in southern Tibet, *Nature*, *307*(5946), 32–36, 1984.
- Fyfe, W. S., N. J. Price, and A. B. Thompson, *Fluids in the Earth's Crust*, pp. 383, Elsevier, New York, 1978.
- Gassman, F., Über die elastizität poröser medien, *V. Nat. Gesellsch.*, *96*, 1–23, 1951.
- Hammer, P. T. C., and R. M. Clowes, Seismic reflection investigations of the Mount Cayley bright spot: A midcrustal reflector beneath the Coast Mountains, British Columbia, *J. Geophys. Res.*, *101*, 20,119–20,131, 1996.
- Harrison, T. M., P. Copeland, W. S. F. Kidd, and A. Yin, Raising Tibet, *Science*, *255*(5052), 1663–1670, 1992.
- Harrison, T. M., P. Copeland, W. S. F. Kidd, and O. M. Lovera, Activation of the Nyainqentanghla Shear Zone: Implications for uplift of the southern Tibetan Plateau, *Tectonics*, *14*(3), 658–676, 1995.
- Hashin, Z., and S. Shtrikman, A variational approach to the elastic behavior of multiphase materials, *J. Mech. Phys. Solids*, *11*, 127–140, 1963.
- Henry, P., X. Le Pichon, and B. Goffe, Kinematic, thermal and petrological model of the Himalayas: Constraints related to metamorphism within the underthrust Indian crust and topographic elevation, *Tectonophysics*, *273*, 31–56, 1997.
- Hirn, A., et al., Crustal structure and variability of the Himalayan border of Tibet, *Nature*, *307*(5946), 23–25, 1984.
- Hirn, A., M. Sapin, J. C. Lepine, J. Diaz, and J. Mei, Increase in melt fraction along south-north traverse below the Tibetan Plateau: Evidence from seismology, *Tectonophysics*, *273*, 17–30, 1997.
- Hochstein, M. P., and K. Regenauer-Lieb, Heat generation associated with collision of two plates: The Himalayan Geothermal belt, *J. Volcanol. Geotherm. Res.*, *83*(1–2), 75–92, 1998.
- Hochstein, M. P., and Z. Yang, Modeling of terrain-induced advective flow in Tibet: Implications for assessment of crustal heat flow, in *Seventh Workshop on Geothermal Reservoir Engineering*, pp. 153–157, Stanford Univ., Calif., 1992.
- Hochstein, M. P., and Z. Yang, Modeling of terrain-induced advective flow in Tibet: Implications for assessment of crustal heat flow, in *Terrestrial Heat Flow and Geothermal Energy in Asia*, edited by M. L. Gupta and M. Yamamoto, pp. 331–368, Oxford and IBH, New Delhi, 1995.
- Hoke, L., S. Lamb, and D. R. Hilton, Helium isotope results from the Tibetan plateau—A tool for understanding active mantle processes beneath southern Tibet, in *11th Himalaya-Karakorum-Tibet Workshop*, edited by A. M. Macfarlane, R. B. Sorkhabi, and J. Quade, pp. 65–66, Flagstaff, Ariz., 1996.
- Holliger, K., Upper-crustal seismic velocity heterogeneity as derived from a variety of P-wave sonic logs, *Geophys. J. Int.*, *125*, 813–829, 1996.
- Hudson, J. A., Wave speed and attenuation of elastic waves in material containing cracks, *Geophys. J. R. Astron. Soc.*, *64*, 133–150, 1981.
- Hussenoeder, S. A., J. A. Collins, G. M. Kent, R. S. Detrick, and TERA-Group, Seismic analysis of the axial magma chamber reflector along the southern East Pacific Rise from conventional reflection profiling, *J. Geophys. Res.*, *101*, 22,087–22,105, 1996.
- Hyndman, R. D., and P. M. Shearer, Water in the lower continental crust: Modeling magnetotelluric and seismic reflection results, *Geophys. J. R. Astron. Soc.*, *98*(2), 343–365, 1989.
- Jahns, R. H., Internal evolution of pegmatite bodies, in *Short Course in Granitic Pegmatites in Science and Industry*, edited by P. Cerny, pp. 293–327, Miner. Assoc. of Canada, Winnipeg, 1982.
- Jarchow, M. J., G. A. Thompson, R. D. Catchings, and W. D. Mooney, Seismic evidence for active magmatic underplating beneath the Basin and Range province, western United States, *J. Geophys. Res.*, *98*, 22,095–22,108, 1993.
- Jones, A. G., Electrical conductivity of the continental lower crust, in *Continental Lower Crust*, edited by D. M. Fountain, R. Arculus, and R. W. Kay, pp. 81–143, Elsevier, New York, 1992.
- Jones, A. G., and K. Holliger, Spectral analysis of the KTB sonic and density logs using robust nonparametric methods, *J. Geophys. Res.*, *102*, 18,391–18,404, 1997.
- Jones, T. D., and A. Nur, The nature of seismic reflections from deep crustal fault zones, *J. Geophys. Res.*, *89*, 3153–3171, 1984.
- Kind, R., J. Ni, W. Zhao, J. Wu, X. Yuan, L. Zhao, E. Sandvol, C. Reese, J. Nabelek, and T. Hearn, Evidence from earthquake data for a partially molten crustal layer in southern Tibet, *Science*, *274*(5293), 1692–1694, 1996.

- Krauskopf, K. B., and D. K. Bird, *Introduction to Geochemistry*, 647 pp., McGraw-Hill, New York, 1995.
- Krief, M., J. Garat, J. Stellingwerff, and J. Ventre, A petrophysical interpretation using the velocities of P and S waves (full-waveform sonic), *Log Anal.*, 31(6), 355–369, 1990.
- Kuster, G. T., and M. N. Toksöz, Velocity and attenuation of seismic waves in two-phase media, 1, Theoretical formulations, *Geophysics*, 39(5), 587–606, 1974.
- Laporte, D., Behavior of crustal melts during crustal anatexis: The distribution of hydrous silicic melts in polycrystalline aggregates of quartz, *Contrib. Mineral. Petrol.*, 116, 486–499, 1994.
- Laporte, D., C. Rapaille, and A. Provost, Wetting angle equilibrium melt geometry, and the permeability threshold of partially molten crustal protoliths, in *Granite: From Segregation of Melt to Emplacement Fabrics*, edited by J. L. Bouchez et al., pp. 31–54, Kluwer Acad., Norwell, Mass., 1997.
- Le Pichon, X., P. Henry, and B. Goffe, Uplift of Tibet: from eclogites to granulites—Implications for the Andean Plateau and the Variscan belt, *Tectonophysics*, 273, 57–76, 1997.
- Lidaka, T., K. Miura, and A. Ikami, Evidence for the existence of a mid-crustal reflector in the Beppu-Shimabara Graben, Kyushu, Japan, *Geophys. Res. Lett.*, 20, 1699–1702, 1993.
- Lüeschen, E., Crustal “bright spots” and anisotropy from multi-component P- and S-wave measurements in southern Germany, *Tectonophysics*, 232(1–4), 343–354, 1994.
- Luth, W. C., R. H. Jahns, and O. F. Tuttle, The granite system at pressure of 4 to 10 kilobars, *J. Geophys. Res.*, 69, 759–773, 1964.
- Makovsky, Y., and S. L. Klemperer, Wide-angle recording in conjunction with Project INDEPTH: velocity structure of Southern Tibet, in *10th Himalaya-Karakoram-Tibet Workshop, Monte Verita, Ascona, Ticino, Switzerland, 4–8 April, 1995, Abstract Volume*, edited by D. A. Spencer, J.-P. Burg, and C. Spencer-Cervato, pp. 264–266, ETH Zürich, Zürich, 1995.
- Makovsky, Y., and S. Klemperer, INDEPTH-2 wide-angle experiment, Tibet 1994; Data for IRIS-PASSCAL archives, data report, IRIS-PASSCAL DMC, Seattle, Wash., 1996.
- Makovsky, Y., S. L. Klemperer, L. Ratschbacher, L. D. Brown, M. Li, W. Zhao, and F. Meng, INDEPTH wide-angle reflection observation of P-wave-to-S-wave conversion from crustal bright spots in Tibet, *Science*, 274(5293), 1690–1691, 1996.
- Mandler, H. A. F., and R. M. Clowes, The Wollaston Lake reflector: a 160 km long “bright spot” in the Precambrian crust of the Trans-Hudson orogen, Canada, in *Deep Seismic Reflection Profiling of the Continents, II: A Global Survey*, edited by S. L. Klemperer and W. D. Mooney, *Tectonophysics*, 288, 71–81, 1998.
- Matsumoto, S., and A. Hasegawa, Distinct S-wave reflector in the midcrust beneath Nikko-Shirane Volcano in the northeastern Japan Arc, *J. Geophys. Res.*, 101, 3067–3083, 1996.
- Mavko, G., Velocity and attenuation in partially molten rocks, *J. Geophys. Res.*, 85, 5173–5189, 1980.
- Mavko, G., T. Mukerji, and J. Dvorkin, *The Rock Physics Handbook*, 300 pp., Cambridge Univ., New York, 1998.
- Molnar, P., and W. Chen, Focal depths and fault plane solutions of earthquakes under the Tibetan plateau, *J. Geophys. Res.*, 88, 6911–6917, 1983.
- Molnar, P., P. Tapponnier, and W. P. Chen, Extensional tectonics in central and eastern Asia; a brief summary, in *Extensional Tectonics Associated With Convergent Plate Boundaries*, edited by F. J. Vine and A. G. Smith, pp. 403–406, Philos. Trans. R. Soc. Lond., London, England, 1981.
- Murase, T., and A. R. McBirney, Properties of some common igneous rocks and their melts at high temperatures, *Geol. Soc. Am. Bull.*, 84(11), 3563–3592, 1973.
- Nelson, K. D., et al., Partially molten middle crust beneath southern Tibet: Synthesis of Project INDEPTH results, *Science*, 274(5293), 1684–1688, 1996.
- O’Connell, R. J., and B. Budiansky, Seismic velocities in dry and saturated cracked solids, *J. Geophys. Res.*, 79, 5412–5426, 1974.
- Ostrander, W. J., Plane-wave reflection coefficients for gas sands at non-normal angles of incidence, *Geophysics*, 49(10), 1637–1648, 1984.
- Owens, T. J., and G. Zandt, Implications of crustal property variations for models of Tibetan plateau evolution, *Science*, 387, 37–43, 1997.
- Pratt, T. L., J. F. Mondary, L. D. Brown, N. I. Christensen, and S. H. Danbom, Crustal structure and deep reflector properties; wide angle shear and compressional wave studies of the midcrustal Surrency bright spot beneath southeastern Georgia, *J. Geophys. Res.*, 98, 17,723–17,735, 1993.
- Rivers, M. L., and I. S. E. Carmichael, Ultrasonic studies of silicate melts, *J. Geophys. Res.*, 92, 9247–9270, 1987.
- Royden, L., Coupling and decoupling of crust and mantle in convergent orogens: Implications for strain partitioning in the crust, *J. Geophys. Res.*, 101, 17,679–17,705, 1996.
- Ryberg, T., and G. S. Fuis, The San Gabriel bright reflective zone: Possible evidence of young mid-crustal thrust faulting in southern California, in *Deep Seismic Reflection Profiling of the Continents, I: General Results and New Methods*, edited by S. L. Klemperer and W. D. Mooney, *Tectonophysics*, 286, 31–46, 1998.
- Sanford, A. R., O. Alptekin, and T. R. Toppozada, Use of reflection phases on microearthquake seismograms to map an unusual discontinuity beneath the Rio Grande Rift, *Bull. Seismol. Soc. Am.*, 63, 2021–2034, 1973.
- Sanford, A. R., R. P. Mott Jr., P. J. Shuleski, E. J. Rinehart, F. J. Caravella, R. M. Ward, and T. C. Wallace, Geophysical evidence for a magma body in the crust in the vicinity of Socorro, New Mexico, in *The Earth’s Crust: Its Nature and Physical Properties*, *Geophys. Monogr. Ser.*, vol. 20, edited by J. G. Heacock, pp. 385–403, AGU, Washington, D. C., 1977.
- Schilling, F. R., G. M. Partzsch, H. Brasse, and G. Schwartz, Partial melting below the magmatic arc in the central Andes deduced from geoelectromagnetic field experiments and laboratory data, *Phys. Earth Planet. Int.*, 103, 17–31, 1997.
- Schmeling, H., Numerical models on the influence of partial melt on elastic, anelastic and electric properties of rocks, I, Elasticity and anelasticity, *Phys. Earth Planet. Int.*, 41, 34–57, 1985.
- Schmidt, H., OASES version 2.0, application and upgrade notes, Dep. of Ocean Eng., Mass. Inst. of Technol., Cambridge, 1996.
- Schmidt, H., and J. Glattet, A fast field model for three-dimensional wave propagation in stratified environments based on the global matrix method, *J. Acoust. Soc. Am.*, 78, 2105–2114, 1985.
- Schmidt, H., and G. Tango, Efficient global matrix approach to the computation of synthetic seismograms, *Geophys. J. R. Astron. Soc.*, 84, 331–359, 1986.
- Shen, X., W. Zhang, S. Yang, and J. Zhang, Abnormal thermal structure and related geothermal resources of the Tibetan plateau, in *Terrestrial Heat Flow and Geothermal Energy in Asia*, edited by M. L. Gupta and M. Yamamoto, pp. 369–387, Oxford and IBH, New Delhi, 1995.
- Sheriff, R. E., and L. P. Geldart, *Exploration Seismology*, 592 pp., Cambridge Univ. Press, New York, 1995.
- Shuey, R. T., A simplification of the Zoeppritz equations, *Geophysics*, 50(4), 609–614, 1985.
- Stocker, R. L., and R. B. Gordon, Velocity and internal friction in partial melts, *J. Geophys. Res.*, 80(35), 4828–4836, 1975.
- Stone, C. B., ‘Bright spot’ techniques, in *Developments in Petroleum Geology*, edited by G. D. Hobson, pp. 275–291, Appl. Sci. Publ., London, 1977.
- Taylor, H. P., Oxygen and hydrogen isotope constraints on the deep circulation of surface waters into zones of hydrothermal metamorphism and melting, in *The Role of Fluids in Crustal Processes*, edited by Geophysics Study Committee, pp. 72–95, Natl. Acad. Press, Washington, D. C., 1990.
- Thompson, A. B., Dehydration melting of pelitic rocks and the generation of H₂O-undersaturated granitic liquids, *Am. J. Sci.*, 282(2), 1567–1595, 1982.
- Thompson, A. B., and J. A. D. Connolly, Metamorphic fluids and anomalous porosities in the lower crust, *Tectonophysics*, 182, 47–55, 1990.
- Toksöz, M. N., B. Mandal, and A. M. Dainty, Frequency-dependent attenuation in the crust, *Geophys. Res. Lett.*, 17(7), 973–976, 1990.
- Vo-Thanh, D., A. Polian, and P. Richet, Elastic properties of silicate melts up to 2350 K from Brillouin scattering, *Geophys. Res. Lett.*, 23(5), 423–426, 1996.
- Wang, J. Y., et al., Geothermal studies in China, *J. Volcanol. Geotherm. Res.*, 9(1), 57–76, 1981.
- Watanabe, T., Effects of water and melt on seismic velocities and their application to characterization of seismic reflectors, *Geophys. Res. Lett.*, 20(24), 2933–2936, 1993.
- Watson, E. B., and J. M. Brenan, Fluids in the lithosphere, 1, Experimentally-determined wetting characteristics of CO₂-H₂O fluids and their implications for fluid transport, host-rock physical properties,

- and fluid inclusion formation, *Earth Planet. Sci. Lett.*, *85*, 497–515, 1987.
- Wickham, S. M., Fluids in the deep crust—Petrological and isotopic evidence, in *Continental Lower Crust*, edited by D. M. Fountain, R. Arculus, and R. W. Kay, pp. 391–422, Elsevier, New York, 1992.
- Willett, S. D., and C. Beaumont, Subduction of Asian lithospheric mantle beneath Tibet inferred from models of continental collision, *Nature*, *369*(6482), 642–645, 1994.
- Wood, B. J., and J. V. Walther, Fluid flow during metamorphism and its implications for fluid-rock ratios, in *Fluid-Rock Interactions During Metamorphism*, edited by J. V. Walther and B. J. Wood, pp. 89–108, Springer-Verlag, New York, 1986.
- Yardley, B. W. D., and J. W. Valley, How wet is the Earth's crust?, *Nature*, *371*, 205–206, 1994.
- Yardley, B. W. D., and J. W. Valley, The petrologic case for a dry lower crust, *J. Geophys. Res.*, *102*, 12,173–12,185, 1997.
- Yardley, G. S., G. Graham, and S. Crampin, Viability of shear-wave amplitude versus offset studies in anisotropic media, *Geophys. J. Int.*, *107*, 493–503, 1991.
- Zhang, X., Isotopic characteristic of thermal fluid and genesis of geothermal water from the Yangbajing geothermal field, Tibet, in *Fifth International Symposium on Water-Rock Interaction, Extended Abstracts*, Orkustofnun Natl. Energy Auth., Reykjavik, Iceland, 1986.
- Zhao, W., K. D. Nelson, and Project INDEPTH Team, Deep seismic reflection evidence for continental underthrusting beneath southern Tibet, *Nature*, *366*, 557–559, 1993.
- Zhu, L., and D. V. Helmberger, Intermediate-depth earthquakes beneath the India-Tibet collision zone, *Geophys. Res. Lett.*, *23*(5), 435–438, 1996.
-
- S. L. Klemperer, Department of Geophysics, Stanford University, Stanford, CA 94305-2215. (sklemp@geo.stanford.edu)
- Y. Makovsky, Paradigm Geophysical, P.O.B. 2061, Herzlia B 46120, Israel. (yizhaq@paradigmgeo.com)

(Received August 1, 1997; revised October 13, 1998; accepted October 21, 1998.)